Industrial Chemistry & Materials



MINI REVIEW

View Article Online



Cite this: Ind. Chem. Mater., 2023, 1,

Received 10th June 2023. Accepted 28th June 2023

DOI: 10.1039/d3im00061c

rsc.li/icm

Core-shell nanostructured magnesium-based hydrogen storage materials: a critical review

Yinghui Li, abc Qiuyu Zhang, Li Ren, abc Zi Li, abc Xi Lin, Care Zhewen Ma, abc Haiyan Yang, ^c Zhigang Hu (D) ^c and Jianxin Zou (D) *abc

Hydrogen holds the advantages of high gravimetric energy density and zero emission. Effective storage and transportation of hydrogen constitute a critical and intermediate link for the advent of widespread applications of hydrogen energy. Magnesium hydride (MgH₂) has been considered as one of the most promising hydrogen storage materials because of its high hydrogen storage capacity, excellent reversibility, sufficient magnesium reserves, and low cost. However, great barriers both in the thermodynamic and the kinetic properties of MgH₂ limit its practical application. Doping catalysts and nanostructuring are two facile but efficient methods to prepare high-performance magnesium (Mg)-based hydrogen storage materials. Core-shell nanostructured Mg-based hydrogen storage materials synergize the strengths of the above two modification methods. This review summarizes the preparation methods and expounds the thermodynamic and kinetic properties, microstructure and phase changes during hydrogen absorption and desorption processes of core-shell nanostructured Mq-based hydrogen storage materials. We also elaborate the mechanistic effects of core-shell nanostructures on the hydrogen storage performance of Mg-based hydrogen storage materials. The goal of this review is to point out the design principles and future research trends of Mq-based hydrogen storage materials for industrial applications.

Keywords: Hydrogen storage; Mg/MgH₂; Core-shell nanostructure; Thermodynamics and kinetics.

^a National Engineering Research Center of Light Alloys Net Forming & State Key Laboratory of Metal Matrix Composites, Shanghai Jiao Tong University, Shanghai, 200240, PR China. E-mail: zoujx@sjtu.edu.cn; Fax: +86 21 34203730;

1 Introduction

Excessive fossil fuel consumption and resultant greenhouse gas (GHG) emissions have led to public health jeopardy and environmental deterioration at the global level. Hydrogen has become one of the most promising alternatives to the current energy landscape because it possesses the highest gravimetric energy density (142 MJ kg⁻¹) among energy carriers.2 The effective development and application of



Yinghui Li

Yinghui Li is a PhD student in the School of Materials Science and Engineering at Shanghai Jiao Tong University. graduated from the South University. His research topic focuses on magnesiumbased hydrogen storage materials.



Jianxin Zou

Jianxin Zou is currently a professor in Materials Science at Shanghai Jiao Tong University in China. He obtained his PhD degrees from the University of Lorraine in France and Dalian University of Technology in 2007. He then served as a postdoctoral fellow at the University of British Columbia. He is now mainly engaged in thedesign, preparation and characterization of advanced magnesium-based energy materials.

^b Shanghai Engineering Research Center of Mg Materials and Applications & School of Materials Science and Engineering, Shanghai Jiao Tong University, Shanghai, 200240 PR China

^c Center of Hydrogen Science, Shanghai Jiao Tong University, Shanghai, 200240, PR China

hydrogen energy mainly needs to solve three scientific problems, i.e., green production, high-density storage and transportation, and efficient conversion of hydrogen. Among them, the development of high-performance hydrogen storage materials is the bottleneck to realize the commercial application of hydrogen energy.3-5 Ideal hydrogen storage materials should fulfill the requirements of (i) high hydrogen storage density, (ii) good hydrogen absorption and desorption kinetics, and (iii) superior cycling stability.6 According to the requirements above, the U.S. Department of Energy (DOE) proposed that the mass density of hydrogen storage should exceed 6 wt%, the hydrogen desorption temperature should be lower than 150 °C, and the cycle life should exceed 1000 times.⁷ The reaction of Mg with hydrogen yields a stable magnesium hydride (MgH2) with a high hydrogen gravimetric and volumetric capacity of 7.6 wt% and 110 g L⁻¹, respectively, abundant magnesium reserves (the earth's magnesium content is about 2.5 wt%), and low cost.8 It has been considered to be one of the most promising hydrogen storage materials. However, there are two major impediments in the practical utilization of a Mg/MgH2 hydrogen storage system: the enthalpy of the hydrogen absorption/desorption is 74.7 kJ mol⁻¹ H₂ and the desorption energy barrier is about 160 kJ mol⁻¹ H₂. Excessively high hydrogen absorption and desorption temperatures together with poor kinetic properties severely limit the practical application of the MgH₂/Mg system for hydrogen storage. 9,10

Many pioneering research studies as well as excellent review articles on improving the performance of the MgH₂/ Mg hydrogen storage system have been published. Methods based on addition of catalysts, 11-14 doping with metals to form alloys, 15,16 and nanocrystallization 17,18 have been applied to tune the dehydriding/hydriding thermodynamic and kinetic performance of Mg/MgH2. Among them, the introduction of catalysts can change the electronic structure of MgH₂/Mg and thus significantly reduce the energy barrier of H2 dissociation. Nanostructured Mg-based materials can shorten the diffusion pathway, which is more conducive to the transport of H atoms, thereby markedly improving the hydrogen absorption and desorption rate of Mg-based hydrogen storage materials. For example, Xia et al. synthesized graphene-supported MgH2 nanoparticles covered homogeneous nanosized Ni catalysts. 19 nanoparticles are homogenously distributed throughout the surface and between the layers of graphene, which provides geometric confinement of the MgH2 nanoparticles to suppress agglomeration during the thermal hydrogen storage process. The MgH2 nanoparticles could implement hydrogenation within 60 min at 50 °C and release 5.4 wt% hydrogen within 30 min at 250 °C under the catalytic effect of Ni. Zhu et al. successfully fabricated highly dispersed MgH₂ nanoparticles immobilized on 3D Ti-MXenes.²⁰ The MgH2 nanoparticles started to decompose at 140 °C and released 3.0 wt% H2 at 150 °C within 3 h. 3D Ti-MXenes played the role of nanoconfinement and in situ catalysis. Recently, researchers have found that properly designed core–shell nanostructure can improve the overall hydrogen storage performance of Mg-based materials. 6,21-23 The catalytic atoms at the interface of the core–shell nanostructure can react or change the electronic structure of the Mg atoms nearby and form many active sites, 24 where the dissociation, 25 transportation, 26 and recombination of hydrogen atoms can be accelerated. In addition, the shell structure can also serve as a protective layer to prevent the oxidation and agglomeration of nano Mg/MgH2 during the thermal hydrogen storage process. 28 Constructing and optimizing core–shell nanostructures is a promising synthetic strategy to synthesize Mg-based materials for both transportation and stationary applications.

Nevertheless, there are few reviews published in recent years that focus on the relationship between the unique structure and properties of core-shell Mg-based hydrogen storage materials. This paper summarizes the latest research progress of core-shell nanostructured Mg-based hydrogen storage materials, mainly covering an introduction of the preparation methods and technology, advances in material synthesis and mechanistic effects, followed by an outlook on future research studies and applications.

2 Preparation methods of core-shell nanostructured Mg-based hydrogen storage materials

2.1 Ball milling method

Nowadays mechanical milling is one of the most common methods to synthesize and modify core-shell nanostructured Mg-based materials (Fig. 1). 29-32 In this type of preparation, the ball-milled MgH2 and catalysts have a considerably high energy.33 As researched by El-Eskandarany et al., the effective centrifugal force of the composites and balls under ball milling reaches up to 20 times gravitational acceleration.³⁴ The MgH₂ powder particles will reduce their particle size and create fresh surfaces under the abrasive and impacting force. Metals or other materials can be introduced onto the surface MgH₂/Mg under mechanical forces, forming a homogeneous shell. Liu et al. synthesized NiCu nanoparticles anchored on the surface of reduced graphene oxide catalyst (rGO@NiCu) and incorporated it into MgH₂ by ball milling.³⁵ MgH2-rGO@NiCu exhibited good cycling stability during the thermal hydrogen ab/desorption process by the protection of the NiCu/rGO shell. At the same time, the nanocrystalline structure and associated defects form through mechanical milling, which are often perceived as leading to enhanced hydrogen ab/desorption kinetics. However, the core-shell nanostructured Mg-based materials prepared by the highenergy ball milling method usually exhibit uneven thickness and particle size, and wide hydrogen absorption and desorption temperature range. Meanwhile, nanoparticles obtained from ball milling undergo a significant growth in crystal size and a subsequent structural relaxation of defects in the initial hydrogen ab/desorption cycles.

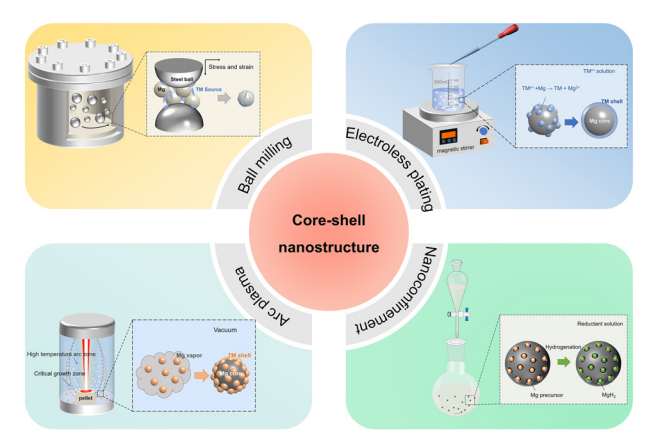


Fig. 1 Preparation methods of core-shell nanostructured Mg-based hydrogen storage materials.

2.2 Electroless plating method

The electroless plating method directly utilizes the strong reducibility of Mg to reduce transition metals with higher electronegativity from the metal salt, which coats on the surface of the Mg nanoparticles *in situ* to form a core–shell structure.³⁶ The electronegativity of Mg is 1.31, which is more negative than that of 3d transition metals. In principle, these metal ions can be deposited on the surface of Mg nanoparticles to form core–shell structures.

Lu et al. used nano magnesium particles prepared by a direct current (DC) arc plasma method as the core and adopted a liquid-phase electroless plating method to prepare Mg@TM (TM = Ti, Co, V) composite materials with core-shell structures. 37,38 The researchers utilized the electroless plating method to fabricate core-shell structures, which usually consists of three steps. Firstly, the TM salts and pure Mg ultrafine powder were evenly dispersed in organic solvents (including THF etc.) separately. Secondly, the TM salt solution was added to the magnesium nanoparticle dispersion proportionally and the mixture was stirred vigorously at room temperature, followed by isolation through centrifugation and repeated rinsing to wash away the residual Mg salt solution. Finally, the core-shell structured Mg@TM composites were obtained by drying the rinsed products under vacuum. Owing to the operation convenience of the electroless plating method, additional metal catalysts can be introduced to the Mg-TM binary core-shell structure to build a multilayer structure. The synergistic effect between metal catalysts can further improve the comprehensive hydrogen storage performance of Mg-based materials. Lu et al. continued to plate a layer of Ni on the Mg-Ti core-shell structure, and the hydrogen storage performance of the prepared ternary hydrogen storage material had been greatly improved.37 The hydrogen desorption enthalpy (69.84 kJ mol⁻¹ H₂) and the hydrogenation activation energy (63.7 kJ mol⁻¹ H₂) values of the ternary composite were also slightly lower than that of the binary composite (76.37 kJ mol⁻¹ H₂ and 72.2 kJ mol⁻¹ H₂, respectively). These improvements in

the hydrogen storage properties of Mg/MgH₂ are mainly attributed to the combined effects of Mg₂Ni/Mg₂NiH₄ acting as a "hydrogen pump" and TiH₂ acting as the activation site. Similarly, the onset dehydrogenation temperature of hydrogenated Mg@Co@V (323 °C) was lower than that of Mg@Co (342 °C) and Mg@V (346 °C) composites with the combined effects of Mg_xCo/Mg_xCoH_y serving as the "hydrogen pump" and V₂H accelerating the dissociation of H₂.³⁸

Electroless plating is a process in which redox chemical reactions occur violently so that a strictly inert atmosphere is required.³⁹ Also, the post-processing is cumbersome due to the generation of by-products. However, this problem can be avoided if the various chemicals produced in the whole reaction process have catalytic effects on the Mg-based hydrogen storage materials. Cui et al. prepared multiplevalence Ti-doped Mg-based core-shell composite materials.²² The catalytic shell was prepared by the chemical reaction between Mg and TiCl₃ in THF solution, which is ~10 nm in thickness and contains multiple-valence Ti including Ti (0), TiH₂ (+2), TiCl₃ (+3) and TiO₂ (+4). The multiple-valence Ti acted as the intermediate and catalytic active site for the electron transfer between Mg2+ and H and thus contributed significantly to the good dehydrogenation performance, which could start to release H2 at about 175 °C and release 5 wt% H2 within 15 min at 250 °C. The chemical reactions involved in the electroless plating method are simple and controlled. Moreover, this method generates a core-shell structure of Mg and transition metals in situ, which is more conducive to the interactions between Mg and transition metals, and forms an active interface to facilitate hydrogen diffusion.

2.3 Arc plasma method

Arc plasma is an effective physical vapor deposition technology to prepare metal nanoparticles. 40,41 The main process is to use arc plasma to heat the metal block, and then metal evaporation, followed by nucleation and deposition onto a substrate. In the arc plasma process, the sample is evaporated instantaneously. The sample particles continue to grow in the high-temperature growth zone. When the particle is out of the critical temperature zone of growth, the size of the sample particles becomes stable and begins to settle down. In the arc equipment, the temperature gradient is large, and the metal vapor is in a great supersaturation state with the sudden drop of temperature. The metal atoms are difficult to diffuse in a long distance, thus forming the metal nano powders. When the arc vaporizes multiple metals, magnesium with a low melting point will nucleate first, and the nucleus of other transition metals or their compounds attached to the Mg nanoparticles form a shell subsequently, of which the total layer thickness is between a few nanometers and few tens of nanometers due to the low concentration.

The arc plasma method is suitable for forming core-shell nanostructured Mg-based materials coated by different metals or compounds. Magnesium powder can be mixed evenly with metal or its compound powder, which is solidified with a tablet press, and then arced to prepare powder. Zou et al. prepared Mg-RE (RE = La, Nd, Gd, Er) composite powders using an arc plasma evaporation apparatus followed by *in situ* passivation in air. Ultrafine Mg-RE particles were covered by the nano-sized MgO and REO_x shell. 42-44 The hydrogen absorption kinetics of Mg can be significantly improved; in addition, the Mg-RE composite powders showed better anti-oxidation ability than pure Mg powders. Mao et al. prepared core-shell nanostructured Mg- MF_x (M = V, Ni, La and Ce) nanocomposites via the arc plasma method.45 Mg-NiF2 composite showed the best hydrogen absorption properties, which could absorb 3.26 wt% H2 at 100 °C in 2 h. The improved dehydrogenation and hydrolysis properties of the hydrogenated Mg-MF_x composites were attributed to the MgF₂ and metal oxide shell structure. Yang et al. introduced three metal oxides (Al₂O₃, TiO₂ and Fe₂O₃) into Mg ultrafine powders by the arc plasma method to prepare core-shell nanostructured Mg-MOx (M = Al, Ti, Fe) nanocomposites. 46,47 It is worth noting that some metals and magnesium will undergo alloying reactions during the arc plasma process, while some metal compounds will react with magnesium during the arc process to form a shell structure with multiple components.

The arc plasma method has the advantages of low equipment cost, simple operation, fast evaporation speed and high yield, so it is highly convenient for large-scale production. However, there are many variables affecting the size of sample particles, which are related not only to the raw material but also to the current, voltage, distance between the electrodes and the internal atmosphere. Therefore, further optimization of the technical schemes and parameters is required.

2.4 Nanoconfinement method

Nanoconfinement is a modification method of confining Mg/ MgH₂ in porous matrix materials, which effectively limit the movement, agglomeration and growth of nanoparticles.⁶ The size of the Mg/MgH2 can be effectively controlled so as to achieve outstanding hydrogen storage performances. The supporting materials mainly include carbon materials (e.g. ordered mesoporous carbon scaffolds, carbon nanotubes, graphene, etc.), metal-organic frameworks (MOFs), porous polymer materials, covalent organic frameworks (COFs), and so on.⁵⁰ A wet impregnation method was developed by infiltrating the porous scaffold hosts with a solution of magnesium precursor, and the magnesium precursor can enter spontaneously into the channel under capillary force. 51,52 Through subsequent hydrogenation or reduction, the magnesium precursor will transform to MgH2 or Mg nanoparticles confined in the supporting materials. The size of magnesium nanoparticles prepared by nanoconfinement

is closely interrelated with the pore size of the supporting materials. Generally, the scaffolds should be stable under the loading and thermal process of hydrogen release and uptake, and relatively light to hold a high gravimetric hydrogen storage capacity for the composite system. In the composites, magnesium or magnesium hydride obtained by hydrogenation is confined in a nanoporous scaffold shell to form the core–shell nanostructures.

The use of nanoporous supporting materials is a feasible method to limit the particle agglomeration and growth of Mg/MgH₂, which also maintains close contact between the Mg/MgH₂ nanoparticles and scaffolds.⁵³ At the same time, different kinds of supporting materials can give different properties to the resultant composites. A supporting material with catalytic activities can facilitate the desorption and absorption rate of hydrogen. Ren *et al.* utilized 1D N-doped hierarchically porous carbon as the scaffold for MgH₂/Ni nanoparticles.⁵⁴ The Ni nanocrystals on the shell facilitated the formation of Mg₂Ni/Mg₂NiH₄, which acted as the "hydrogen pump" to accelerate the dissociation of hydrogen and recombination of H atoms, and the porous carbon shell suppressed the growth and agglomeration of MgH₂ nanoparticles in the process of hydrogen ab/desorption.

3 Core-shell nano magnesium-based hydrogen storage materials

3.1 Mg@transition metal

Catalyst doping has been regarded as one of the most feasible means to improve the ab/dehydrogenation kinetics of MgH₂ because it can effectively lower the ab/ dehydrogenation energy barrier of Mg/MgH2 systems.55 High H₂ dissociation energy on the surface of Mg and the slow diffusion rate of hydrogen atoms in the MgH2 matrix hinder the reaction kinetics. Transition metals and rare earth elements are ideal catalysts for Mg-based hydrogen storage materials, which can significantly improve the hydrogen absorption and desorption kinetic properties. Firstly, the contact surface between some transition metals and Mgbased hydrogen storage materials will promote the dissociation of hydrogen molecules and produce a large hydrogen solubility gradient through the "spillover effect", thus accelerating the diffusion of hydrogen atoms. Secondly, some metal elements can react with magnesium to form a kind of alloy or corresponding hydrides, which serve as a "hydrogen pump" to provide channels for hydrogen atoms to diffuse into the magnesium matrix. At the same time, the stability of magnesium hydride will be weakened, and the system onset hydrogen desorption temperature will decrease. Therefore, many researchers have prepared core-shell nanostructured Mg@transition metals, i.e., transition metal (TM) as the shell layer, and systematically explored their hydrogen storage performance reaction mechanism.14,56,57

Zou *et al.* synthesized Fe-covered core–shell nanostructured composites and the hydrogen absorption

activation energy was reduced to 54.6 kJ mol⁻¹ H₂.⁵⁸ Subsequently, Lu et al. prepared core-shell structured Mg@TM (TM = Ni, Co, V or Ti) by the plasma method combined with electroless plating method. 37,38 In order to clarify the core-shell structure, TEM observations were employed and the images are shown in Fig. 2a and b. A homogeneous thin layer with a thickness in nanometers was observed on the surface of MgH2 particles, and the sharp peaks at the two sides of the concentration profiles of EDS linear scanning indicated that TM was rich at the edge of hydrogenated Mg@TM particles. Similarly, Lu et al. attempted to use transition metals and Mg nanoparticles to form a ternary core-shell composite system (Mg@Co@V) (Fig. 2c), and the research showed that the ternary magnesium-based hydrogen storage material phase exerted a lower reaction enthalpy and activation energy compared with binary hydrogen storage materials (Fig. 2d).38 Yao and his coworkers coated Mg with TM (TM = Ti, Nb, V, Co, Mo or Ni) and its compounds through high-energy pre-milling Mg powder with the corresponding chlorides (TiCl₃, NbCl₅, VCl₃, CoCl2, MoCl3, and NiCl2) followed by electroless plating technology to form a composite material with Mg as the core and the corresponding TM as the shell.²³ The Mg-Ti composite showed the best hydrogen storage performance among them. Studies showed that metals with lower electronegativity possessed a higher catalytic activity for Mg nanoparticles (Fig. 2e and f). Noble metals also showed a high catalytic activity for Mg-based hydrogen storage materials. Lu et al. prepared the core-shell nanostructured Mg@Pt material by a plasma-solid reaction method.⁵⁹ In situ TEM observations and density functional theory calculations showed that metastable H stabilized the Mg₃Pt particles formed on the interface and acted as a "hydrogen pump" to accelerate the hydrogen absorption and desorption rate of Mg/MgH2.

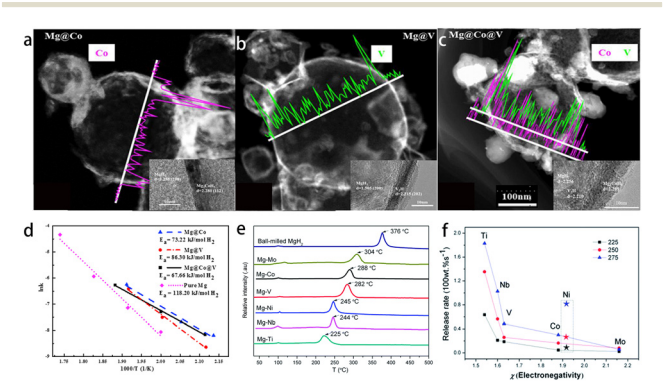


Fig. 2 HAADF-STEM images and elemental line scanning of EDS analysis for hydrogenated (a) Mg@Co, (b) Mg@V and (c) Mg@Co@V composites and (d) the corresponding hydrogen absorption kinetic fitting curves³⁸ (copyright 2017 Elsevier). Comparison in (e) TPD-MS curve rate of 4 K min⁻¹ and (f) dehydrogenation average kinetics within 5 min at different temperatures of Mq-TM samples²³ (copyright 2013 Royal Society of Chemistry).

3.2 Mg@metal oxide

Metal oxide is another kind of catalyst having great potential to improve the hydrogen storage properties of magnesiumbased materials. In the process of hydrogen absorption and desorption, metal oxides can react with magnesium to produce a fast diffusion channel for H atoms, thus accelerating the process of hydrogen absorption and desorption of materials. The excellent kinetic catalytic performance of metal oxides has been widely proved. 60-62 Zou et al. prepared nanosized single-crystal hexagonal Mg particles with a size of 50-600 nm by the plasma method. In situ passivation technology was used to coat a 10-20 nm layer of MgO shell to protect the inner Mg from oxidation. 42 In order to improve the thermodynamics and kinetics of the hydrogen absorption and desorption performance of nano-Mg, rare earth metal oxides as catalysts and protective agents were used to prepare a series of core-shell nanostructured $Mg@ER_2O_3$ ($ER_2O_3 = Ce_2O_3$, La_2O_3 , Er_2O_3 , Gd_2O_3 , Nd_2O_3) with a 20 nm-thick shell of ER2O3.43 Mg@La2O3 (Fig. 3a) showed the best hydrogen storage performances. The total amount of hydrogen absorbed by Mg@La2O3 within 2 h at 200 °C was 5.98 wt%, while pure Mg particles absorbed only 1.8 wt% hydrogen under the same conditions (Fig. 3b and c). Zou et al. also tried to construct ternary core-shell Mg-TM-La (TM = Ti, Fe, Ni) composites by using an arc plasma evaporation apparatus (Fig. 3d).63 The experimental results showed that the hydrogen storage performance of the Mg-TM-La system was better than that of the binary Mg-TM or

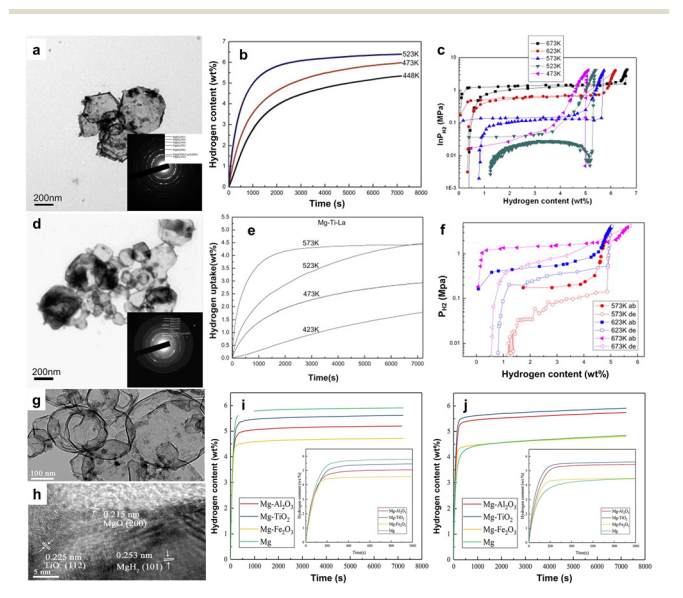


Fig. 3 (a) Bright-field TEM micrograph and the corresponding SAED patterns, (b) hydrogen absorption profiles, and (c) PCT curves of the Mg-La-O composite⁴² (copyright 2012 Elsevier). (d) Bright-field TEM micrograph and the corresponding SAED patterns, (e) hydrogen absorption profiles, and (f) PCT curves of the Mg-La-Ti-O composite⁶³ (copyright 2013 Elsevier). (g) Typical TEM image of the passivated Mg-TiO₂ hydrogenated powder and its (h) HRTEM images; hydrogen absorption profiles for $Mq-MO_x$ (M = Al, Ti and Fe) as well as Mqpowders without (i) and with (j) passivation⁴⁷ (copyright 2019 Elsevier).

Mg-La system (Fig. 3e and f). In the above experiments, metal oxides were formed from magnesium, transition metals and rare earth metals in the passivation process, and the composites exhibited good anti-air oxidizing ability. However, in the passivation process, the oxidation of magnesium will lead to the decrease of the overall hydrogen storage capacity, and the formed magnesium oxide shell will hinder the diffusion of hydrogen atoms, thus reducing the hydrogen absorption and release rate. Yang et al. introduced three metal oxides (Al₂O₃, TiO₂ and Fe₂O₃) into Mg ultrafine powders via the arc plasma method to synthesize core-shell structured Mg-MO_r (M = Al, Ti and Fe) nanocomposites (Fig. 3g and h).47 After passivation treatment, Mg-TiO₂ exhibited a higher hydrogen absorption capacity (5.90 wt%) than pure Mg (4.85 wt%), which resulted from the good protective and catalytic effect of TiO2 on the hydrogen absorption process of Mg (Fig. 3i and j). In addition, the direct addition of metal oxides greatly enriched the types of Mg@TMOx core-shell structured composites.

3.3 Mg@carbon

Studies have shown that the hydrogen absorption and desorption performances of the composite can be significantly improved by ball milling CNTs mixed with magnesium hydrides.⁶⁴ However, compared with most metal catalysts, the improvement of carbon on the kinetic performance of magnesium hydrides is relatively weak. Carbon materials have many advantages of low density, light weight, lower cost, high stability and easy adjustability.65 A variety of porous carbon materials have been designed to act as catalyst support materials or as scaffold materials for magnesium hydrides. Mg/MgH2 is dispersed in the pores of the carbon matrix, forming a unique core-shell structure with Mg/MgH2 as the core and carbon as the shell. Besides improved thermodynamic and kinetic performance, Mg@carbon core-shell nanostructures have other unique features, such as air tolerance and cyclic stability. Jeon et al. used PMMA, which could allow hydrogen to pass but blocks oxygen and water molecules (Fig. 4a), to nano-confine Mg and prepare a Mg-PMMA core-shell structure composite material, and studied the hydrogen absorption and desorption properties of the material.66 Microstructural analyses revealed the presence of Mg particles with an average diameter of 5 nm (Fig. 4b). The material could achieve a reversible cycle at 200 °C, had a fast hydrogen absorption rate, and could absorb 4 wt% hydrogen within 30 min. At the same time, PMMA could effectively prevent the oxidation and agglomeration of Mg/ MgH₂ and maintain the hydrogen storage performance (Fig. 4c). Eun Seon Cho et al. constructed Mg nanocrystals encapsulated by atomically thin and gas-selective reduced graphene oxide (rGO) sheets (Fig. 4d and e).67 As the rGO shell was atomically thin, this approach could minimize inactive mass in the composite, which exhibited

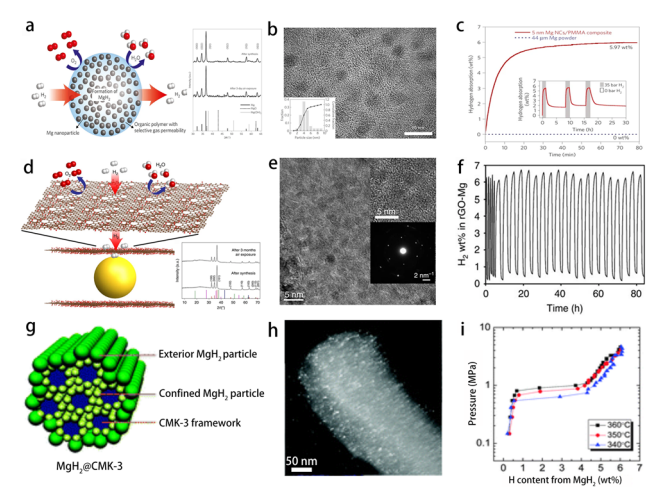


Fig. 4 (a) Sketch of high-capacity Mg nanoparticles encapsulated by a selectively gas-permeable polymer composite, corresponding X-ray diffraction patterns of the as-synthesized structure (top) and after three days of air-exposure; (b) HRTEM micrograph of the assynthesized structure; (c) hydrogen absorption and desorption properties of Mg nanoparticles/PMMA⁶⁶ (copyright 2011 Springer Nature). (d) Illustrations depicting the structure of rGO-Mg, corresponding XRD spectra of rGO-Mg after synthesis and after 3 months in air and (e) HRTEM micrograph of as-synthesized rGO-Mg; (f) hydrogen absorption/desorption cycling of rGO-Mg⁶⁷ (copyright 2016 Springer Nature). (g) Schematic model of MgH2@CMK-3 composite and its (h) HADDF-STEM image; (i) PCT isotherms for H2 absorption in MqH₂@CMK-3⁶⁸ (copyright 2013 Royal Society of Chemistry).

exceptionally dense hydrogen storage (6.5 wt% and 0.105 kg H₂ L⁻¹) (Fig. 4f). This material was also protected from oxygen and moisture by the rGO layers. Jia et al. used CMK-3 to prepare a MgH₂@CMK-3 core-shell structured composite (Fig. 4g) with a MgH2 size ranging from 1 to 2 nm without any bulk phase formation (Fig. 4h).68 Such nanoconfined MgH2 within CMK-3 could alter the thermodynamic property of MgH₂ (Fig. 4i), thereby reducing the desorption temperature. The results confirmed that the desorption temperature threshold of confined MgH2 could be lowered to 50 °C. The charge transfer from MgH2 to the carbon shell played a critical role in the observed lowtemperature dehydrogenation. In addition, activated carbon and carbon aerogel scaffold were selected to confine MgH2 nanoparticles to explore the kinetic properties of hydrogen uptake and release and other properties. 69,70

3.4 Other core-shell structured Mg-based composites

In addition to the metals, metal oxides and carbon materials described above, metal carbides, fluorides and other composites are also often introduced into Mg-based hydrogen storage materials to construct core-shell nanostructures. Hu et al. confined TiCx-embedded Mg core in 2–3 nm carbon shells through a gas evaporation method.⁷¹ The Mg₈₈(TiC_{0.6})₁₂@C nanocomposite could absorb 5.5 wt% H₂ within 25 min at 250 °C and desorb 4.5 wt% H₂ within 60 min at 300 °C. Mao et al. prepared core-shell nanostructured Mg@metal fluoride (MF $_x$, M = V, Ni, La and Ce) composites

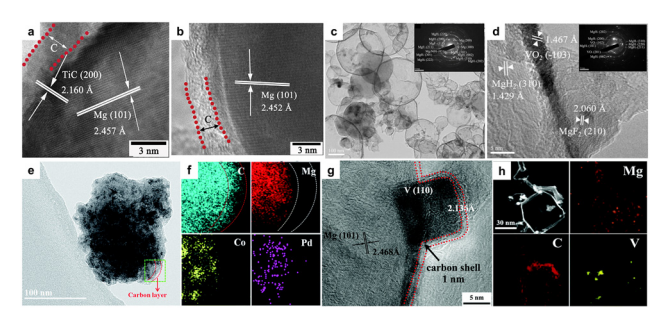


Fig. 5 HRTEM micrograph of (a) Mg $_{96}$ (TiC) $_{4}$ @C and (b) Mg $_{75}$ (TiC $_{0.6}$) $_{25}$ @C 71 nanocomposites (copyright 2020 Elsevier). (c) TEM bright-field images of the hydrogenated Mg-NiF $_{2}$ composite; (d) HRTEM image of the hydrogenated Mg-VF $_{3}$ and the corresponding SAED pattern 45 (copyright 2017 Elsevier). TEM images and EDS profiles of (e and f) MgH $_{2}$ -Co/Pd@B-CNTs 30 (copyright 2019 Royal Society of Chemistry) and (g and h) Mg $_{92}$ V $_{8}$ @C 77 composites (copyright 2019 Royal Society of Chemistry).

via the arc plasma method (Fig. 5c and d). ⁴⁵ MF_x could improve both the hydrogen absorption performance of Mg and the hydrolysis properties of relevant hydrogenated powder.

MOFs have considerable surface areas, ordered mesoporous structures, and potential catalytic effects (due to metal ions), which means that they can be designed as multifunctional host materials for nanoconfinement of Mg/MgH₂.^{72,73} Ma *et al.* successfully prepared a Ni(π)-based MOF (Ni-MOF) scaffold by a solvothermal method to nano-confine MgH₂.⁷⁴ Owing to the nano-cofine and catalytic effects of the Ni-MOF, the core–shell structured MgH₂@Ni-MOF composite showed excellent hydrogen sorption thermodynamic and kinetic performances. The derivates of MOFs with high surface areas and metal catalytic sites can also serve as functionalized scaffolds.⁷⁵

A composite shell structure can be designed in order to hydrogen storage materials with comprehensive performance. Adding metal catalysts to Mg@carbon composites is a good way to further enhance the hydrogen storage properties.⁷⁶ Liu et al. found that the addition of carbon materials to Mg-based composites was conducive to the formation of a core-shell structure with MgH₂ as the core by ball milling (Fig. 5e and f).³⁰ Studies have shown that the carbon shell can inhibit the of particles, improving the kinetic agglomeration performance of the material. MgH₂-Co/Pd@B-CNTs composites can absorb 6.68 wt% hydrogen within 10 s at 250 °C and also have a fast hydrogen absorption rate at low temperatures. Lotoskyy et al. also found that after graphite was added to the Mg-Ti system by high-energy ball milling, the graphite evenly covered the surface of MgH2.77 The Mgbased hydrogen storage material with graphite had better stability, even after 100 weeks, and the hydrogen absorption/ desorption rate and hydrogen storage capacity remained nearly unchanged. Chen et al. constructed a Mg-V-C hydrogen storage composite with an average size of 32 nm

and with carbon material as the shell by vapor deposition (Fig. 5g and h).⁷⁸ The thickness of the carbon shell of this material is 1 nm; therefore, the hydrogen storage capacity of this material is relatively high, which can maintain a hydrogen storage capacity of 5.2 wt%. Different components contained in composites can play different catalytic roles in some aspects of thermodynamics, kinetics, cycling and other properties of core–shell nanostructured Mg-based hydrogen storage materials. In addition, synergistic catalysis between different components can show better catalytic effect than single catalysts.⁷⁹ The hydrogen storage performances of typical core–shell nanostructured Mg-based materials are summarized in Table 1.

4 Mechanistic effects of core-shell nanostructure

4.1 Thermodynamic and kinetic principles of MgH₂ for hydrogen storage

4.1.1 Thermodynamics of the Mg/MgH₂ system. The hydrogen absorption reaction of Mg generates the corresponding hydride of MgH₂, which can be written as:

$$Mg + H_2 \Rightarrow MgH_2.$$
 (1)

The equilibrium of the three phases above refers to the composition, temperature and hydrogen pressure. ⁸⁰ At a fixed temperature and reference pressure ($p^0 = 1$ bar), the standard Gibbs free energy change of reaction (1) is eqn (2):

$$\Delta G^0 = \Delta H^0 - T \Delta S^0 = -RT \ln \frac{p^0}{p_{\rm H_2}^{\rm eq}}.$$
 (2)

Correspondingly, the Gibbs free energy of the hydriding reaction is eqn (3):

$$\Delta G = \Delta H - T \Delta S = RT \ln \frac{p_{\rm H_2}^{\rm eq}}{p_{\rm H_2}}, \tag{3}$$

where T is the absolute temperature, R the universal gas constant ($R = 8.314 \text{ J mol}^{-1} \text{ K}^{-1}$), p_{H_2} the plateau pressure at the temperature, and ΔH and ΔS the enthalpy and entropy change of the hydrogen absorption, respectively.

When $p_{\rm H_2} > p_{\rm H_2}^{\rm eq}$, $\Delta G < 0$, the hydriding reaction is thermodynamically favoured, and reversely, the dehydriding reaction happens. Notably, $p_{\rm H_2}^{\rm eq}$ is closely related with the temperature, so the driving force of reaction (1) depends on both temperature and $p_{\rm H_2}$.

4.1.2 Kinetics of the Mg/MgH₂ system. According to the thermodynamic analysis above, under the hydrogen pressure of 1 bar, MgH₂ begins to decompose at about 280 °C. However, the desorption temperature of unmodified MgH₂ is higher than 350 °C. This is because both thermodynamics and kinetics restrict the practical operation temperature of the Mg/MgH₂ system.

The hydrogen absorption processes of Mg mainly contain four steps: H₂ adsorption, H₂ splitting, H chemisorption and

Table 1 Hydrogen storage performances of typical core-shell nanostructured Mg-based materials

	Material	Synthetic method	Ab/desorption activation energy (kJ mol^{-1} H_2)	Hydrogen storage properties	Ref.
Mg-Nb Electroless plating −/48.2 Ab ± 2.8 wf9/250 °C/12 MPa/5 min De: 2.8 wf9/250 °C/12 MPa/5 min De: 1.1 wf9/250 °C/12 MPa/5 min De: 0.7 wf9/250 °C/12 MPa/5 min De: 0.7 wf9/250 °C/12 MPa/5 min De: 0.7 wf9/550 °C/12 MPa/5 min De: 2.0 wf9/550 °C/12 MPa/5 min De: 2.0 wf9/550 °C/12 MPa/5 min De: 2.0 wf9/550 °C/12 MPa/5 min De: 0.5 wf9/5250 °C/12 MPa/10 min Mg-Co Electroless plating 7.2.2/− Ab: 2.2 wf9/6250 °C/2.8 MPa/10 min Mg-Co Ab: 2.2 wf9/6250 °C/2.8 MPa/10 min Mg-Co Electroless plating 8.3.7− Ab: 3.7 wf9/250 °C/2.8 MPa/10 min Mg-Co Blectroless plating 8.3.7− Ab: 3.7 wf9/250 °C/2.8 MPa/10 min Mg-Mg-Ni-Ti Blectroless plating 8.3.7− Ab: 3.4 wf9/250 °C/2.8 MPa/10 min Mg-Mg-Ni-Ti Blectroless plating 6.7.7− Ab: 3.9 wf9/6250 °C/2.8 MPa/10 min Mg-Mg-Ni-Ti Mg-Ni-Ti Blectroless plating 6.7.7− Ab: 3.9 wf9/6250 °C/2.8 MPa/10 min Mg-Mg-Ni-Ti Mg-Ni-Ti Ab: 2.4 wf9/6250 °C/2.8 MPa/10 min Mg-Mg-Ni-Ti Mg-Ni-Ti Ab: 3.9 wf9/6250 °C/2.8 MPa/10 min Mg-Mg-Ni-Ti Mg-Ni-Ti Ab: 3.9 wf9/6250 °C/2.8 MPa/10 min Mg-Mg-Ni-Ti Mg-Ni-Ti Ab: 3.8 wf9/6250 °C/2.8 MPa/10 min Mg-Mg-Ni-Ti Mg-La ₀ O ₁ Are plasma & passivation 7.9/− Ab: 3.4 wf	Mg-Ti	Electroless plating	/30.9	Ab: 4.1 wt%/225 °C/2 MPa/5 min	23
Mg-V Electroless plating	-			De: 4.6 wt%/250 °C/1 kPa/10 min	
Mg-V Electroless plating —/56.5	Mg-Nb	Electroless plating	/48.2	Ab: 4.2 wt%/225 °C/2 MPa/5 min	23
Mg-V Electroless plating —/56.5		1 8		De: 2.5 wt%/250 °C/1 kPa/10 min	
De: 1.1 wt%/250 °C/1 kPa/10 min	Mg-V	Electroless plating	 /56.5		23
Mg-Ni Electroless plating		1 8			
Dec. 0.7 wt% 250 °C/1 kPa/10 min Mg-Mo	Mg-Ni	Electroless plating	/51.2		23
Mg-Co Electroless plating —/65.4 Ab: 4.0 wt%/252 °C/1 MPa/5 min De: 2.0 wt%/250 °C/1 kPa/10 min Mg-Mo Electroless plating —/76.1 Ab: 3.0 wt%/250 °C/2 MPa/5 min De: 2.0 wt%/250 °C/2 MPa/5 min Mg-Ti Ab: 2.2 wt%/250 °C/2 MPa/5 min De: 0.5 wt%/250 °C/2 MPa/5 min Mg-Co Electroless plating 73.2/— Ab: 3.7 wt%/250 °C/2 MPa/5 min Mg-Co Ab: 3.7 wt%/250 °C/2.8 MPa/10 min Mg-V Electroless plating 86.3/— Ab: 5.0 wt%/250 °C/2.8 MPa/10 min Mg-V Electroless plating 86.3/— Ab: 5.0 wt%/250 °C/2.8 MPa/10 min Mg-V Ab: 4.7 wt%/250 °C/2.8 MPa/10 min Mg-V Electroless plating 67.7/— Ab: 3.7 wt%/250 °C/2.8 MPa/10 min Mg-V Electroless plating 67.7/— Ab: 3.9 wt%/250 °C/2.8 MPa/10 min Mg-V Mg-Vision Pa/250 °C/2.8 MPa/10 min Mg-Vision Pa/250 °C/2.8 MPa/250 min Mg-Vision Pa/250 °C/2.8 MPa/250 min Mg-Vision Pa/250 °C/2 Mpa/250 °C/2 Mpa/2		1 8			
De: 2.0 wf%/250 °C/1 kPa/10 min Mg-Mo	Мg-Со	Electroless plating	/65.4		23
Mg-Mo Electroless plating −/76.1 Ab: 3.0 wt%/252 °C/2 MPa/5 min Dev: 0.5 wt%/250 °C/1.8 MPa/10 min Mg-Co Electroless plating 72.2/− Ab: 2.2 wt%/250 °C/2.8 MPa/10 min Mg-Co Electroless plating 73.2/− Ab: 3.7 wt%/250 °C/2.8 MPa/10 min Mg-Co Ab: 3.7 wt%/250 °C/2.8 MPa/10 min Mg-Co Ab: 5.0 wt%/250 °C/2.8 MPa/10 min Mg-Co Ab: 5.0 wt%/250 °C/2.8 MPa/10 min Mg-Mg-Co-V Electroless plating 86.3/− Ab: 4.7 wt%/250 °C/2.8 MPa/10 min Mg-Mg-Co-V Ab: 4.7 wt%/250 °C/2.8 MPa/10 min Mg-Mg-Ni-Ti Electroless plating 63.7/− Ab: 3.9 wt%/250 °C/2.8 MPa/10 min Mg-Mg-MgO Are plasma & passivation 55.9/− Ab: 3.1 wt%/300 °C/3.5 MPa/15 min Mg-Mg-MgO Are plasma & passivation 42.0/− Ab: 3.1 wt%/300 °C/3 MPa/15 min Mg-Mg-Ng-Og Are plasma & passivation 55.9/− Ab: 3.4 wt%/300 °C/3 MPa/15 min Mg-Mg-Ng-Og Are plasma & passivation 55.9/− Ab: 5.3 wt%/300 °C/3 MPa/15 min Mg-Mg-Ng-Og Are plasma & passivation 55.9/− Ab: 5.4 wt%/300 °C/3 MPa/15 min Mg-Mg-Ng-Og Are plasma & passivation 55.9/− Ab: 5.0 wt%/300 °C/3 Mpa/15 min Mg-Mg-Ng-Og Are plasma & passivation 57.9/− Ab: 6.0 wt%/300 °C/3 Mpa/15 min Mg-Ng-Ng-Og Are plasma & passivation 58.7/− Ab: 6.0 wt%/300 °C/3 Mpa/15 min Mg-Ng-Ng-Ng-Ng-Ng-Ng-Mg-Ng-Mg-Mg-Mg-Mg-Mg-Mg-Mg-Mg-Mg-Mg-Mg-Mg-Mg		7 8			
De: 0.5 wt%/250 °C/1 kPa/10 min Mg-Ti	Мд-Мо	Electroless plating	—/76 . 1		23
Mg-Ti Electroless plating 72.2/— Ab: 2.2 wt%/250 °C/2.8 MPa/10 min Mg-Co Electroless plating 73.2/— Ab: 3.7 wt%/250 °C/2.8 MPa/10 min Mg-V Electroless plating 86.3/— Ab: 5.0 wt%/250 °C/2.8 MPa/10 min Mg-Ni Electroless plating 88.9/— Ab: 4.7 wt%/250 °C/2.8 MPa/10 min Mg-Ni-Ti Electroless plating 67.7/— Ab: 3.9 wt%/250 °C/2.8 MPa/10 min Mg-Ni-Ti Electroless plating 63.7/— Ab: 2.5 wt%/250 °C/2.8 MPa/10 min Mg-Ni-Ti Electroless plating 63.7/— Ab: 3.1 wt%/250 °C/2.8 MPa/10 min Mg-Ni-Ti Electroless plating 63.7/— Ab: 2.5 wt%/250 °C/2.8 MPa/10 min Mg-MgO Arc plasma & passivation 55.9/— Ab: 3.1 wt%/300 °C/3.5 MPa/10 min Mg-La ₂ O ₃ Arc plasma & passivation 55.9/— Ab: 3.1 wt%/300 °C/3.5 MPa/15 min Mg-Nd ₂ O ₃ Arc plasma & passivation 59.3/— Ab: 5.3 wt%/300 °C/4 MPa/5 min Mg-Er ₂ O ₃ Arc plasma & passivation 79.9/— Ab: 5.3 wt%/300 °C/4 MPa/5 min Mg-H ₂ O ₃ Arc plasma & passivation 79.9/— Ab: 5.6 wt%/300 °C/4 MPa/5 min Mg-H ₂ O ₃ Arc plasma & passivation 79.9/— Ab: 5.6 wt%/300 °C/3 Mpa/100 s Mg-Al ₂ O ₃ Arc plasma & passivation 79.9/— Ab: 5.6 wt%/300 °C/3 Mpa/5 min Mg-TiO ₂ Arc plasma & passivation 38.8/— Ab: 5.6 wt%/300 °C/3 Mpa/5 min Mg-La ₂ O ₃ -Ti Arc plasma & passivation 38.8/— Ab: 5.6 wt%/300 °C/3 Mpa/20 min Mg-La ₂ O ₃ -Ti Arc plasma & passivation 34.7/— Ab: 3.8 wt%/300 °C/3 Mpa/20 min Mg-La ₂ O ₃ -Ti Arc plasma & passivation 74.5/— Ab: 3.8 wt%/300 °C/3 Mpa/20 min Mg-La ₂ O ₃ -Ti Arc plasma & passivation 74.5/— Ab: 3.8 wt%/300 °C/3 Mpa/20 min Mg-La ₂ O ₃ -Ti Arc plasma & passivation 74.5/— Ab: 3.8 wt%/300 °C/3 Mpa/20 min Mg-La ₂ O ₃ -Ti Arc plasma & passivation 74.5/— Ab: 3.8 wt%/300 °C/3 Mpa/20 min Mg-La ₂ O ₃ -Ti Arc plasma & passivation 74.5/— Ab: 3.8 wt%/300 °C/3 Mpa/20 min Mg-La ₂ O ₃ -Ti Arc plasma & passivation 74.5/— Ab: 3.5 wt%/300 °C/3 Mpa/20 min Mg-La ₂ O ₃ -Ti Arc plasma & passivation 74.5/— Ab: 3.5 wt%/300 °C/3 Mpa/20 min Mg-La ₂ O ₃ -Ti Arc plasma & passivation 74.5/— Ab: 3.5 wt%/300 °C/3 Mpa/20 min Mg-La ₂ O ₃ -Ti Arc plasma Passivation 74.5/— Ab: 5.5 wt%/300 °C/3 Mpa/20 min Mg-La ₂ O ₃ -Ti A		8	,		
Mg-Co Electroless plating 73.2/— Ab: 3.7 wf%/250 °C/2.8 MPa/10 min Mg-V Electroless plating 86.3/— Ab: 5.0 wf%/250 °C/2.8 MPa/10 min Mg-Ni Electroless plating 86.3/— Ab: 4.7 wf%/250 °C/2.8 MPa/10 min Mg-Ni Electroless plating 67.7/— Ab: 3.9 wf%/250 °C/2.8 MPa/10 min Mg-Ni-Ti Electroless plating 67.7/— Ab: 3.9 wf%/250 °C/2.8 MPa/10 min Mg-Ni-Ti Ab: 3.1 wf%/250 °C/2.8 MPa/10 min Mg-Ni-Ti Ab: 5.2 wf%/300 °C/3 MPa/5 min Mg-Ni-Ti Ab: 5.3 wf%/300 °C/3 MPa/5 min Mg-Ni-Ti Ab: 5.2 wf%/300 °C/4 MPa/5 min Mg-Ni-Ti Ab: 5.2 wf%/300 °C/4 MPa/5 min Mg-Yi-Ti Ab: 5.2 wf%/300 °C/3 Mpa/20 min Mg-Yi-Ti Ab: 5.4 wf%/325 °C/3 Mpa/5 min Mg-Yi-Ti Ab: 5.6 wf%/325 °C/3 Mpa/20 min Mg-Yi-Ti Ab: 5.6 wf%/300 °C/0 Mpa/20 min Mg-Yi-Ti Ab: 5.2 w	Mg-Ti	Electroless plating	72.2/—		37
Mg-V Electroless plating 86.3/— Ab: 5.0 w/96/250 °C/2.8 MPa/10 min Mg-Ni Electroless plating 88.9/— Ab: 4.7 wt%/250 °C/2.8 MPa/10 min Mg-Co-V Electroless plating 67.7/— Ab: 3.9 wt%/250 °C/2.8 MPa/10 min Mg-Ni-Ti Electroless plating 63.7/— Ab: 2.5 wt%/250 °C/2.8 MPa/10 min Mg-MgO Arc plasma & passivation 42.0/— Ab: 4.8 wt%/250 °C/3.5 MPa/15 min Mg-La ₂ O ₃ Arc plasma & passivation 55.9/— Ab: 5.3 wt%/300 °C/4 MPa/5 min Mg-Gd ₂ O ₃ Arc plasma & passivation 59.3/— Ab: 6.0 wt%/300 °C/4 MPa/5 min Mg-Ft ₂ O ₃ Arc plasma & passivation 79.9/— Ab: 5.4 wt%/300 °C/4 MPa/5 min Mg-H ₂ O ₃ Arc plasma & passivation 79.9/— Ab: 5 wt%/300 °C/3 Mpa/5 min Mg-TiO ₂ Arc plasma 48.0/— Ab: 5.2 wt%/320 °C/3 Mpa/5 min Mg-TiO ₂ Arc plasma 48.0/— Ab: 5.2 wt%/300 °C/3 Mpa/20 min Mg-La ₂ O ₃ —Ti Arc plasma & passivation 34.7/— Ab: 3.8 wt%/300 °C/3 MPa/20 min Mg-La ₂ O ₃ —Ni Arc plasma 42.0/— Ab: 3.8 wt%/300 °C/3 MPa/120 min Mg-La ₂ O ₃ —Ni Arc plasma 72.4/139.2					38
Mg−Ni Electroless plating 88.9/— Ab: 4.7 wt%/250 °C/2.8 MPa/10 min Mg−Co−V Electroless plating 67.7/— Ab: 3.9 wt%/250 °C/2.8 MPa/10 min Mg−Ni−Ti Electroless plating 63.7/— Ab: 2.5 wt%/250 °C/2.8 MPa/10 min Mg−MgO Arc plasma & passivation 55.9/— Ab: 3.1 wt%/300 °C/3.5 MPa/15 min Mg−La ₂ O ₃ Arc plasma & passivation 42.0/— Ab: 3.1 wt%/300 °C/3.5 MPa/15 min Mg−Nd ₂ O ₃ Arc plasma & passivation 55.9/— Ab: 5.3 wt%/300 °C/4 MPa/5 min Mg−Nd ₂ O ₃ Arc plasma & passivation 55.9/— Ab: 5.3 wt%/300 °C/4 MPa/5 min Mg−Nd ₂ O ₃ Arc plasma & passivation 59.3/— Ab: 5.3 wt%/300 °C/4 MPa/5 min Mg−Nd ₂ O ₃ Arc plasma & passivation 78.7/— Ab: 5.2 wt%/300 °C/4 MPa/5 min Mg−Nd ₂ O ₃ Arc plasma & passivation 78.7/— Ab: 5.0 wt%/300 °C/4 MPa/5 min Mg−Nd ₂ O ₃ Arc plasma & passivation 78.7/— Ab: 5.2 wt%/300 °C/3 Mpa/100 s Ab: 5.2 wt%/300 °C/3 Mpa/100 s Mg−Nd ₂ O ₃ O ₃ O ₃ Arc plasma 48.0/— Ab: 5.2 wt%/300 °C/3 Mpa/100 s Mg−Nd ₂ O ₃		1 0			38
Mg-Co-V Electroless plating 67.7/— Ab: 3.9 wt%/250 °C/2.8 MPa/10 min Mg-Ni-Ti Mg-Ni-Ti Electroless plating 63.7/— Ab: 2.5 wt%/250 °C/2.8 MPa/10 min Mg-MgO Mg-MgO Are plasma & passivation 55.9/— Ab: 3.1 wt%/300 °C/3.5 MPa/5 min Mg-Nd ₂ O ₃ Mg-Nd ₂ O ₃ Are plasma & passivation 55.9/— Ab: 4.8 wt%/250 °C/3.5 MPa/15 min Mg-Nd ₂ O ₃ Mg-Gd ₂ O ₃ Are plasma & passivation 59.3/— Ab: 5.3 wt%/300 °C/4 MPa/5 min Mg-Nd ₂ O ₃ Mg-Gd ₂ O ₃ Are plasma & passivation 78.7/— Ab: 6.0 wt%/300 °C/4 MPa/5 min Mg-Nd ₂ O ₃ Mg-Al ₂ O ₃ Are plasma & passivation 79.9/— Ab: 5. wt%/300 °C/4 MPa/5 min Mg-Nd ₂ O ₃ Mg-Al ₂ O ₃ Are plasma & passivation 79.9/— Ab: 5.0 wt%/300 °C/4 MPa/5 min Mg-Nd ₂ O ₃ Mg-Al ₂ O ₃ Are plasma 48.0/— Ab: 5.6 wt%/325 °C/3 Mpa/5 min Mg-Nd ₂ O ₃ O ₇ Mg-To ₂ O ₃ -Fe Are plasma & passivation 34.7/— Ab: 5.6 wt%/325 °C/3 Mpa/5 min Mg-La ₂ O ₃ -Fe Mg-La ₂ O ₃ -Fe Are plasma & passivation 34.7/— Ab: 3.8 wt%/300 °C/3 MPa/20 min Mg-La ₂ O ₃ -Fe Mg-La ₂ O ₃ -Fe Are plasma & passivation 74.5/— Ab: 3.8 w		1 0			42
Mg−Ni−Ti Electroless plating 63.7/— Ab: 2.5 wt%/250 °C/2.8 MPa/10 min Mg−MgO Mg−MgO Arc plasma & passivation 55.9/— Ab: 3.1 wt%/300 °C/3.5 MPa/15 min Mg−Nd₂O₃ Arc plasma & passivation 42.0/— Ab: 4.8 wt%/250 °C/3.5 MPa/15 min Mg−Nd₂O₃ Arc plasma & passivation 55.9/— Ab: 4.8 wt%/300 °C/4 MPa/5 min Mg−Nd₂O₃ Arc plasma & passivation 55.9/— Ab: 5.3 wt%/300 °C/4 MPa/5 min Mg−Rd₂O₃ Arc plasma & passivation 78.7/— Ab: 6.0 wt%/300 °C/4 MPa/5 min Mg−Rd₂O₃ Arc plasma & passivation 78.7/— Ab: 6.0 wt%/300 °C/4 MPa/5 min Mg−Rd₂O₃ Arc plasma & passivation 79.9/— Ab: 5.2 wt%/300 °C/3 Mpa/100 s Mg−Rd₂O₃ Arc plasma & passivation 79.9/— Ab: 5.2 wt%/325 °C/3 Mpa/5 min Mg−Rd₂O₃ Mg−Rd₂O₃ Arc plasma & passivation 79.9/— Ab: 5.2 wt%/325 °C/3 Mpa/5 min Mg−Rd₂O₃ Mg−Rd₂O₃—Tin Arc plasma & passivation 79.9/— Ab: 5.6 wt%/325 °C/3 Mpa/5 min Mg−Rd₂O₃—Tin Arc plasma & passivation 74.7/— Ab: 5.6 wt%/325 °C/3 Mpa/20 min Mg−Rd₂O₃—Tin Arc plasma & passivation 74.7/— Ab: 3.8 wt%/300 °C/3 MPa/20 min Mg−Rd₂O₃—Tin Arc plasma & passivation 74.5/— Ab: 3.8 wt%/300 °C/3 MPa/120 min Mg−Rd₂O₃—Tin Arc plasma 72.4/139.2 Ab: 5.2 wt%/200 °C/3 MPa/120 min Mg−Rd₂O₃—Tin Arc plasma 73.0/185.8 Ab: 6.2 wt%/200 °C/3 MPa/120 min Mg−Rd₂O₃—Tin Arc plasma 75.6.5 Ab: 5.3 wt%/200 °C/3 MPa/120 min Mg−Rd₂O₃—Tin Arc pla	-	1 0			38
Mg-MgO Are plasma & passivation 55.9/— Ab: 3.1 wt%/300 °C/3.5 MPa/5 min Mg-La₂O₃ Are plasma & passivation 42.0/— Ab: 4.8 wt%/250 °C/3.5 MPa/15 min Mg-Gd₂O₃ Are plasma & passivation 55.9/— Ab: 5.3 wt%/300 °C/4 MPa/5 min Mg-Gd₂O₃ Are plasma & passivation 59.3/— Ab: 2.4 wt%/300 °C/4 MPa/5 min Mg-Y₂O₃ Are plasma & passivation 78.7/— Ab: 6.0 wt%/300 °C/3 Mpa/5 min Mg-Y₂O₃ Are plasma & passivation 79.9/— Ab: 5.2 wt%/325 °C/3 Mpa/5 min Mg-Y₂O₃ Are plasma 48.0/— Ab: 5.2 wt%/325 °C/3 Mpa/5 min Mg-La₂O₃-Ti Are plasma & passivation 38.8/— Ab: 5.6 wt%/320 °C/3 MPa/20 min Mg-La₂O₃-Fe Are plasma & passivation 34.7/— Ab: 3.8 wt%/300 °C/3 MPa/20 min Mg-La₂O₃-Fi Are plasma & passivation 74.5/— Ab: 3.8 wt%/300 °C/3 MPa/120 min Mg-La₂O₃-Ni Are plasma & passivation 74.5/— Ab: 3.8 wt%/200 °C/3 MPa/120 min Mg-La₂O₃-Fi Are plasma 73.0/185.8 Ab: 5.2 wt%/200 °C/3 MPa/120 min Mg-La₂O₃-Fi Are plasma 73.0/185.8 Ab: 5.2 wt%/200 °C/3 MPa/120 min Mg-La₂O₃-Fi Are plasma 112.	U	1 0			37
Mg-La₂O₃ Are plasma & passivation 42.0/— Ab: 4.8 wt%/250 °C/3.5 MPa/15 min Mg-Nd₂O₃ Are plasma & passivation 55.9/— Ab: 5.3 wt%/300 °C/4 MPa/5 min Mg-Gd₂O₃ Are plasma & passivation 59.3/— Ab: 2.4 wt%/300 °C/4 MPa/5 min Mg-Gd₂O₃ Are plasma & passivation 78.7/— Ab: 6.0 wt%/300 °C/4 MPa/5 min Mg-Y₂O₃ Are plasma & passivation 79.9/— Ab: 5 wt%/300 °C/3 Mpa/100 s Mg-Ha₂O₃ Are plasma 52.3/— Ab: 5.6 wt%/325 °C/3 Mpa/5 min Mg-TiO₂ Are plasma 48.0/— Ab: 5.6 wt%/325 °C/3 Mpa/5 min Mg-La₂O₃-Ti Are plasma & passivation 38.8/— Ab: 3.8 wt%/300 °C/3 MPa/20 min Mg-La₂O₃-Ni Are plasma & passivation 74.5/— Ab: 3.8 wt%/300 °C/3 MPa/20 min Mg-Ni-La₂O₃-Ni Are plasma & passivation 74.5/— Ab: 3.8 wt%/200 °C/3 MPa/120 min Mg-LaF₃ Are plasma 73.0/185.8 Ab: 6.2 wt%/200 °C/3 MPa/120 min Mg-VF₃ Are plasma 73.0/185.8 Ab: 6.2 wt%/200 °C/3 MPa/120 min Mg-VF₃ Are plasma 75.5 Ab: 5.2 wt%/200 °C/3 MPa/120 min Mg-VF₃ Are plasma 756.5 Ab: 5.4 wt%/200 °C/3 MPa/120 m	0	1 0			41
Mg-Nd ₂ O ₃ Arc plasma & passivation 55.9/— Ab: 5.3 wt%/300 °C/4 MPa/5 min Mg-Gd ₂ O ₃ Arc plasma & passivation 78.7/— Ab: 6.0 wt%/300 °C/4 MPa/5 min Mg-Er ₂ O ₃ Arc plasma & passivation 79.9/— Ab: 5 wt%/300 °C/3 Mpa/100 s Mg-Al ₂ O ₃ Arc plasma & passivation 79.9/— Ab: 5 wt%/300 °C/3 Mpa/100 s Mg-Al ₂ O ₃ Arc plasma 48.0/— Ab: 5.6 wt%/325 °C/3 Mpa/5 min Mg-La ₂ O ₃ -Ti Arc plasma & passivation 38.8/— Ab: 3.8 wt%/300 °C/3 MPa/20 min Mg-La ₂ O ₃ -Fe Arc plasma & passivation 34.7/— Ab: 3.8 wt%/300 °C/3 MPa/20 min Mg-La ₂ O ₃ -Ti Arc plasma & passivation 74.5/— Ab: 3.8 wt%/300 °C/3 MPa/20 min Mg-La ₂ O ₃ -Ti Arc plasma & passivation 74.5/— Ab: 3.8 wt%/300 °C/3 MPa/120 min Mg-La ₂ O ₃ -Ti Arc plasma & passivation 74.5/— Ab: 3.8 wt%/200 °C/3 MPa/120 min Mg-La ₂ O ₃ -Ni Arc plasma 72.4/139.2 Ab: 5.2 wt%/200 °C/3 MPa/120 min Mg-CeF ₃ Arc plasma 73.0/185.8 Ab: 6.2 wt%/200 °C/3 MPa/120 min Mg-VF ₃ Arc plasma 112.6/204.5 Ab: 5.3 wt%/200 °C/3 MPa/120 min Mg-Ni-Ti ₃ C ₂	0 0				42
Mg-Gd ₂ O ₃ Arc plasma & passivation 59.3/— Ab: 2.4 wt%/300 °C/4 MPa/5 min Mg-F ₂ O ₃ Arc plasma & passivation 78.7/— Ab: 6.0 wt%/300 °C/4 MPa/5 min Mg-Y ₂ O ₃ Arc plasma & passivation 79.9/— Ab: 5 wt%/300 °C/3 Mpa/100 s Mg-Al ₂ O ₃ Arc plasma 52.3/— Ab: 5.2 wt%/325 °C/3 Mpa/5 min Mg-TiO ₂ Arc plasma & passivation 38.8/— Ab: 5.6 wt%/325 °C/3 Mpa/20 min Mg-La ₂ O ₃ -Ti Arc plasma & passivation 34.7/— Ab: 3.8 wt%/300 °C/3 MPa/20 min Mg-La ₂ O ₃ -Fe Arc plasma & passivation 34.7/— Ab: 3.8 wt%/300 °C/3 MPa/20 min Mg-La ₂ O ₃ -Ti Arc plasma & passivation 34.7/— Ab: 3.8 wt%/200 °C/3 MPa/20 min Mg-La ₂ O ₃ -Ti Arc plasma & passivation 74.5/— Ab: 3.8 wt%/200 °C/3 MPa/120 min Mg-La ₂ O ₃ -Ti Arc plasma & passivation 74.5/— Ab: 3.8 wt%/200 °C/3 MPa/120 min Mg-La ₂ O ₃ -Ti Arc plasma 72.4/139.2 Ab: 5.2 wt%/200 °C/3 MPa/120 min Mg-CeF ₃ Arc plasma 66.2/182.4 Ab: 5.3 wt%/200 °C/3 MPa/120 min Mg-VF ₃ Arc plasma 112.6/204.5 Ab: 5.5 wt%/200 °C/3 MPa/120 min Mg-Ni-Ti ₃ C ₂	0				43
Mg-Er₃O₃ Arc plasma & passivation 78.7/— Ab: 6.0 wt%/300 °C/4 MPa/5 min Mg-Y₂O₃ Arc plasma & passivation 79.9/— Ab: 5 wt%/300 °C/3 Mpa/100 s Mg-Al₂O₃ Arc plasma 52.3/— Ab: 5.2 wt%/325 °C/3 Mpa/5 min Mg-TiO₂ Arc plasma 48.0/— Ab: 5.6 wt%/325 °C/3 Mpa/5 min Mg-La₂O₃-Ti Arc plasma & passivation 38.8/— Ab: 3.8 wt%/300 °C/3 MPa/20 min Mg-La₂O₃-Fe Arc plasma & passivation 34.7/— Ab: 3.8 wt%/300 °C/3 MPa/20 min Mg-La₂O₃-Fi Arc plasma & passivation 74.5/— Ab: 3.8 wt%/200 °C/3 MPa/20 min Mg-NiF₂ Arc plasma & passivation 74.5/— Ab: 3.8 wt%/200 °C/3 MPa/120 min Mg-NiF₂ Arc plasma 73.0/185.8 Ab: 5.2 wt%/200 °C/3 MPa/120 min Mg-CeF₃ Arc plasma 73.0/185.8 Ab: 5.3 wt%/200 °C/3 MPa/120 min Mg-VF₃ Arc plasma 112.6/204.5 Ab: 5.3 wt%/200 °C/3 MPa/120 min Mg-TiC₂ Arc plasma 112.6/204.5 Ab: 4.1 wt%/200 °C/3 MPa/120 min Mg-TiC₂ Ball milling -/56.5 Ab: 5.5 wt%/200 °C/1 kPa/60 min Mg-Ni-Ti₃C₂ Ball milling /76.7 Ab: 6.5 wt%/200 °C/2 kPa/30 min					43
Mg-Y₂O₃ Arc plasma & passivation 79.9/— Ab: 5 wt%/300 °C/3 Mpa/100 s Mg-Al₂O₃ Arc plasma 52.3/— Ab: 5.2 wt%/325 °C/3 Mpa/100 s Mg-Ta₂O₃ Ti Arc plasma & passivation 38.8/— Ab: 5.6 wt%/325 °C/3 Mpa/5 min Mg-La₂O₃ Ti Arc plasma & passivation 34.7/— Ab: 3.8 wt%/300 °C/3 MPa/20 min Mg-La₂O₃ Fe Arc plasma & passivation 74.5/— Ab: 3.8 wt%/200 °C/3 MPa/20 min Mg-La₂O₃ Ni Arc plasma & passivation 74.5/— Ab: 3.8 wt%/200 °C/3 MPa/120 min Mg-La₂O₃ Ni Arc plasma 72.4/139.2 Ab: 5.2 wt%/200 °C/3 MPa/120 min Mg-LaF₃ Arc plasma 73.0/185.8 Ab: 5.2 wt%/200 °C/3 MPa/120 min Mg-CeF₃ Arc plasma 73.0/185.8 Ab: 5.3 wt%/200 °C/3 MPa/120 min Mg-VF₃ Arc plasma 112.6/204.5 Ab: 5.3 wt%/200 °C/3 MPa/120 min Mg-VF₃ Arc plasma 112.6/204.5 Ab: 5.5 wt%/200 °C/3 MPa/120 min Mg-Ni-Ti₃C₂ Ball milling 56/73 Ab: 5.4 wt%/125 °C/3 MPa/25 s De: 5.2 wt%/250 °C/2 kPa/15 min Mg-CoPd-CNT Ball milling /76.7 Ab: 6.5 wt%/250 °C/2 kPa/30 min Mg-Ni-Cu-rGO Ball milling -/71.7 <td>-</td> <td></td> <td></td> <td></td> <td>43</td>	-				43
Mg-Al ₂ O ₃ Arc plasma 52.3/— Ab: 5.2 wt%/325 °C/3 Mpa/5 min Mg-TiO ₂ Arc plasma 48.0/— Ab: 5.6 wt%/325 °C/3 Mpa/5 min Mg-La ₂ O ₃ -Ti Arc plasma & passivation 38.8/— Ab: 3.8 wt%/300 °C/3 MPa/20 min Mg-La ₂ O ₃ -Fe Arc plasma & passivation 34.7/— Ab: 3.8 wt%/300 °C/3 MPa/20 min Mg-La ₂ O ₃ -Ni Arc plasma & passivation 74.5/— Ab: 3.8 wt%/200 °C/3 MPa/20 min Mg-NiF ₂ Arc plasma 72.4/139.2 Ab: 5.2 wt%/200 °C/3 MPa/120 min Mg-LaF ₃ Arc plasma 73.0/185.8 Ab: 5.2 wt%/200 °C/3 MPa/120 min Mg-VF ₃ Arc plasma 66.2/182.4 Ab: 5.3 wt%/200 °C/3 MPa/120 min Mg-VF ₃ Arc plasma 112.6/204.5 Ab: 4.1 wt%/200 °C/3 MPa/120 min Mg-TiC _x Arc plasma 15.5 wt%/250 °C/4 MPa/25 min Mg-Ni-Ti ₃ C ₂ Ball milling 56/73 Ab: 5.4 wt%/125 °C/3 MPa/20 s Mg-CoPd-CNT Ball milling /76.7 Ab: 6.5 wt%/250 °C/2 kPa/15 min Mg-NiCu-rGO Ball milling /76.7 Ab: 5.0 wt%/250 °C/2 kPa/30 min Mg-V-C Reactive gas evaporation 41/67 Ab: 5.5 wt%/200 °C/3 MPa/40 min					
Mg-TiO₂ Arc plasma 48.0/— Ab: 5.6 wt%/325 °C/3 Mpa/5 min Mg-La₂O₃-Ti Arc plasma & passivation 38.8/— Ab: 3.8 wt%/300 °C/3 MPa/20 min Mg-La₂O₃-Fe Arc plasma & passivation 34.7/— Ab: 3.8 wt%/300 °C/3 MPa/20 min Mg-La₂O₃-Ni Arc plasma & passivation 74.5/— Ab: 3.8 wt%/200 °C/3 MPa/20 min Mg-NiF₂ Arc plasma 72.4/139.2 Ab: 5.2 wt%/200 °C/3 MPa/120 min Mg-LaF₃ Arc plasma 73.0/185.8 Ab: 6.2 wt%/200 °C/3 MPa/120 min Mg-CeF₃ Arc plasma 66.2/182.4 Ab: 5.3 wt%/200 °C/3 MPa/120 min Mg-VF₃ Arc plasma 112.6/204.5 Ab: 4.1 wt%/200 °C/3 MPa/120 min Mg-TiC₂ Arc plasma —/56.5 Ab: 5.5 wt%/250 °C/4 MPa/25 min Mg-Ni-Ti₃C₂ Ball milling 56/73 Ab: 5.4 wt%/125 °C/3 MPa/25 s Mg-Ni-Ti₃C₂ Ball milling /76.7 Ab: 6.5 wt%/200 °C/2 kPa/15 min Mg-CoPd-CNT Ball milling /76.7 Ab: 6.5 wt%/200 °C/2 kPa/30 min Mg-NiCu-rGO Ball milling -/71.7 Ab: 5.0 wt%/250 °C/2 kPa/20 min Mg-V-C Reactive gas evaporation 41/67 Ab: 5.5 wt%/200 °C/3 MPa/45 min	0 - "			-	44
Mg-La₂O₃-Ti Arc plasma & passivation 38.8/— Ab: 3.8 wt%/300 °C/3 MPa/20 min Mg-La₂O₃-Fe Arc plasma & passivation 34.7/— Ab: 3.8 wt%/300 °C/3 MPa/20 min Mg-La₂O₃-Ni Arc plasma & passivation 74.5/— Ab: 3.8 wt%/200 °C/3 MPa/20 min Mg-NiF₂ Arc plasma 72.4/139.2 Ab: 5.2 wt%/200 °C/3 MPa/120 min Mg-LaF₃ Arc plasma 73.0/185.8 Ab: 6.2 wt%/200 °C/3 MPa/120 min Mg-CeF₃ Arc plasma 66.2/182.4 Ab: 5.3 wt%/200 °C/3 MPa/120 min Mg-VF₃ Arc plasma 112.6/204.5 Ab: 4.1 wt%/200 °C/3 MPa/120 min Mg-TiC₂ Arc plasma -/56.5 Ab: 5.5 wt%/250 °C/4 MPa/25 min Mg-Ni-Ti₃C₂ Ball milling 56/73 Ab: 5.4 wt%/125 °C/3 MPa/125 s De: 5.2 wt%/250 °C/2 kPa/15 min Mg-CoPd-CNT Ball milling /76.7 Ab: 6.5 wt%/200 °C/8 MPa/20 s De: 6.3 wt%/250 °C/2 kPa/30 min Mg-NiCu-rGO Ball milling -/71.7 Ab: 5.0 wt%/200 °C/3 MPa/100 s De: 5.0 wt%/200 °C/4 MPa/45 min Mg-V-C Reactive gas evaporation 41/67 Ab: 5.5 wt%/200 °C/4 MPa/45 min Mg-PMMA Nanoconfinement 25/79 Ab: 6.5 wt%/200 °C/1.5 MPa/45 min <tr< td=""><td>· - ·</td><td>-</td><td></td><td>-</td><td>47</td></tr<>	· - ·	-		-	47
Mg-La ₂ O ₃ -Fe Arc plasma & passivation 34.7/— Ab: 3.8 wt%/300 °C/3 MPa/20 min Mg-La ₂ O ₃ -Ni Arc plasma & passivation 74.5/— Ab: 3.8 wt%/200 °C/3.5 MPa/20 min Mg-NiF ₂ Arc plasma 72.4/139.2 Ab: 5.2 wt%/200 °C/3 MPa/120 min Mg-LaF ₃ Arc plasma 73.0/185.8 Ab: 6.2 wt%/200 °C/3 MPa/120 min Mg-CeF ₃ Arc plasma 66.2/182.4 Ab: 5.3 wt%/200 °C/3 MPa/120 min Mg-VF ₃ Arc plasma 112.6/204.5 Ab: 4.1 wt%/200 °C/3 MPa/120 min Mg-TiC _x Are plasma 112.6/204.5 Ab: 5.5 wt%/250 °C/4 MPa/125 min Mg-Ni-Ti ₃ C ₂ Ball milling 56.5 Ab: 5.5 wt%/250 °C/2 kPa/15 min Mg-CoPd-CNT Ball milling 76.7 Ab: 6.5 wt%/200 °C/8 MPa/20 s Mg-NiCu-rGO Ball milling 776.7 Ab: 5.0 wt%/250 °C/2 kPa/30 min Mg-V-C Reactive gas evaporation 41/67 Ab: 5.5 wt%/200 °C/3 MPa/145 min Mg-PMMA Nanoconfinement 25/79 Ab: 4 wt%/200 °C/3.5 MPa/60 min Mg-GO Nanoconfinement 60.8/92.9 Ab: 6.5 wt%/200 °C/1.5 MPa/45 min	-			•	47
Mg-La ₂ O ₃ -Ni Are plasma & passivation 74.5/— Ab: 3.8 wt%/200 °C/3.5 MPa/20 min Mg-NiF ₂ Are plasma 72.4/139.2 Ab: 5.2 wt%/200 °C/3 MPa/120 min Mg-LaF ₃ Are plasma 73.0/185.8 Ab: 6.2 wt%/200 °C/3 MPa/120 min Mg-CeF ₃ Are plasma 66.2/182.4 Ab: 5.3 wt%/200 °C/3 MPa/120 min Mg-VF ₃ Are plasma 112.6/204.5 Ab: 4.1 wt%/200 °C/3 MPa/120 min Mg-TiC _x Are plasma -/56.5 Ab: 5.5 wt%/250 °C/4 MPa/25 min Mg-Ni-Ti ₃ C ₂ Ball milling 56/73 Ab: 5.4 wt%/125 °C/3 MPa/25 s De: 5.2 wt%/250 °C/2 kPa/15 min Mg-CoPd-CNT Ball milling /76.7 Ab: 6.5 wt%/200 °C/2 kPa/30 min Mg-NiCu-rGO Ball milling -/71.7 Ab: 5.0 wt%/250 °C/2 kPa/30 min Mg-V-C Reactive gas evaporation 41/67 Ab: 5.5 wt%/200 °C/3 MPa/45 min Mg-PMMA Nanoconfinement 25/79 Ab: 4 wt%/200 °C/3.5 MPa/60 min Mg-GO Nanoconfinement 60.8/92.9 Ab: 6.5 wt%/200 °C/1.5 MPa/45 min					63
Mg-NiF2 Arc plasma 72.4/139.2 Ab: 5.2 wt%/200 °C/3 MPa/120 min Mg-LaF3 Arc plasma 73.0/185.8 Ab: 6.2 wt%/200 °C/3 MPa/120 min Mg-CeF3 Arc plasma 66.2/182.4 Ab: 5.3 wt%/200 °C/3 MPa/120 min Mg-VF3 Arc plasma 112.6/204.5 Ab: 4.1 wt%/200 °C/3 MPa/120 min Mg-TiCx Arc plasma -/56.5 Ab: 5.5 wt%/250 °C/4 MPa/25 min Mg-Ni-Ti3C2 Ball milling 56/73 Ab: 5.4 wt%/125 °C/3 MPa/25 s Mg-CoPd-CNT Ball milling /76.7 Ab: 6.5 wt%/200 °C/2 kPa/15 min Mg-NiCu-rGO Ball milling -/71.7 Ab: 5.0 wt%/250 °C/2 kPa/30 min Mg-V-C Reactive gas evaporation 41/67 Ab: 5.5 wt%/200 °C/3 MPa/45 min Mg-PMMA Nanoconfinement 25/79 Ab: 4 wt%/200 °C/3.5 MPa/60 min Mg-GO Nanoconfinement 60.8/92.9 Ab: 6.5 wt%/200 °C/1.5 MPa/45 min	-				63
Mg-LaF3 Arc plasma 73.0/185.8 Ab: 6.2 wt%/200 °C/3 MPa/120 min Mg-CeF3 Arc plasma 66.2/182.4 Ab: 5.3 wt%/200 °C/3 MPa/120 min Mg-VF3 Arc plasma 112.6/204.5 Ab: 4.1 wt%/200 °C/3 MPa/120 min Mg-TiCx Arc plasma -/56.5 Ab: 5.5 wt%/250 °C/4 MPa/25 min Mg-Ni-Ti3C2 Ball milling 56/73 Ab: 5.4 wt%/125 °C/3 MPa/25 s Mg-CoPd-CNT Ball milling /76.7 Ab: 6.5 wt%/200 °C/8 kPa/15 min Mg-NiCu-rGO Ball milling -/71.7 Ab: 5.0 wt%/250 °C/2 kPa/30 min Mg-V-C Reactive gas evaporation 41/67 Ab: 5.5 wt%/200 °C/3 MPa/45 min Mg-PMMA Nanoconfinement 25/79 Ab: 4 wt%/200 °C/3.5 MPa/60 min Mg-GO Nanoconfinement 60.8/92.9 Ab: 6.5 wt%/200 °C/1.5 MPa/45 min					63
$ \begin{array}{cccccccccccccccccccccccccccccccccccc$	-	1			45
$ \begin{array}{cccccccccccccccccccccccccccccccccccc$		1			45
$\begin{array}{cccccccccccccccccccccccccccccccccccc$		1			45
$\begin{array}{cccccccccccccccccccccccccccccccccccc$		-			45
$ \begin{array}{llllllllllllllllllllllllllllllllllll$	$Mg-TiC_x$	Arc plasma	/56.5		71
De: 5.2 wt%/250 °C/2 kPa/15 min					
Mg-CoPd-CNT Ball milling /76.7 Ab: 6.5 wt%/200 °C/8 MPa/20 s De: 6.3 wt%/250 °C/2 kPa/30 min Mg-NiCu-rGO Ball milling —/71.7 Ab: 5.0 wt%/200 °C/3 MPa/100 s De: 5.0 wt%/275 °C/5 kPa/20 min Mg-V-C Reactive gas evaporation 41/67 Ab: 5.5 wt%/200 °C/4 MPa/45 min De: 5.2 wt%/300 °C/0.1 kPa/60 min Mg-PMMA Nanoconfinement 25/79 Ab: 4 wt%/200 °C/3.5 MPa/60 min Mg-GO Nanoconfinement 60.8/92.9 Ab: 6.5 wt%/200 °C/1.5 MPa/45 min		Ball milling	56/73		84
De: 6.3 wt%/250 °C/2 kPa/30 min Mg–NiCu-rGO Ball milling —/71.7 Ab: 5.0 wt%/200 °C/3 MPa/100 s De: 5.0 wt%/275 °C/5 kPa/20 min Mg–V–C Reactive gas evaporation 41/67 Ab: 5.5 wt%/200 °C/4 MPa/45 min De: 5.2 wt%/300 °C/0.1 kPa/60 min Mg-PMMA Nanoconfinement 25/79 Ab: 4 wt%/200 °C/3.5 MPa/60 min Mg-GO Nanoconfinement 60.8/92.9 Ab: 6.5 wt%/200 °C/1.5 MPa/45 min				De: 5.2 wt%/250 °C/2 kPa/15 min	
Mg-NiCu-rGO Ball milling —/71.7 Ab: 5.0 wt%/200 °C/3 MPa/100 s De: 5.0 wt%/275 °C/5 kPa/20 min Mg-V-C Reactive gas evaporation 41/67 Ab: 5.5 wt%/200 °C/4 MPa/45 min De: 5.2 wt%/300 °C/0.1 kPa/60 min Mg-PMMA Nanoconfinement 25/79 Ab: 4 wt%/200 °C/3.5 MPa/60 min Mg-GO Nanoconfinement 60.8/92.9 Ab: 6.5 wt%/200 °C/1.5 MPa/45 min		Ball milling	/76.7	Ab: 6.5 wt%/200 °C/8 MPa/20 s	30
De: 5.0 wt%/275 °C/5 kPa/20 min				De: 6.3 wt%/250 °C/2 kPa/30 min	
Mg-V-C Reactive gas evaporation 41/67 Ab: 5.5 wt%/200 °C/4 MPa/45 min De: 5.2 wt%/300 °C/0.1 kPa/60 min De: 5.2 wt%/300 °C/0.1 kPa/60 min Mg-PMMA Mg-PMMA Nanoconfinement 25/79 Ab: 4 wt%/200 °C/3.5 MPa/60 min Ab: 6.5 wt%/200 °C/1.5 MPa/45 min De: 5.2 wt%/200 °C/1.5 MPa/45 min Mg-GO		Ball milling	/71.7	Ab: 5.0 wt%/200 °C/3 MPa/100 s	35
De: 5.2 wt%/300 °C/0.1 kPa/60 min Mg-PMMA Nanoconfinement 25/79 Ab: 4 wt%/200 °C/3.5 MPa/60 min Mg-GO Nanoconfinement 60.8/92.9 Ab: 6.5 wt%/200 °C/1.5 MPa/45 min				De: 5.0 wt%/275 °C/5 kPa/20 min	
Mg-PMMA Nanoconfinement 25/79 Ab: 4 wt%/200 °C/3.5 MPa/60 min Mg-GO Nanoconfinement 60.8/92.9 Ab: 6.5 wt%/200 °C/1.5 MPa/45 min	Mg-V-C	Reactive gas evaporation	41/67	Ab: 5.5 wt%/200 °C/4 MPa/45 min	78
Mg-GO Nanoconfinement 60.8/92.9 Ab: 6.5 wt%/200 °C/1.5 MPa/45 min				De: 5.2 wt%/300 °C/0.1 kPa/60 min	
	Mg-PMMA	Nanoconfinement	25/79	Ab: 4 wt%/200 °C/3.5 MPa/60 min	66
Det 6.1 wt/%/200 °C/0 kPa/60 min	Mg-GO	Nanoconfinement	60.8/92.9	Ab: 6.5 wt%/200 °C/1.5 MPa/45 min	67
DC. 0.1 WC/0/300 C/0 KFa/00 HIIII				De: 6.1 wt%/300 °C/0 kPa/60 min	
Mg-Ni-MOF Nanoconfinement 41.5/144.7 Ab: 1.2 wt%/150 °C/3 MPa/60 min	Mg-Ni-MOF	Nanoconfinement	41.5/144.7		68
De: 1.5 wt%/325 °C/2 kPa/150 s				De: 1.5 wt%/325 °C/2 kPa/150 s	

H diffusion.⁸¹ Accordingly, the desorption processes of MgH₂ include the breakage of Mg–H, the diffusion of H, the recombination of H₂ and the physical desorption of H₂. Each step needs to overcome the reaction activation energy barrier (E_a), and a lower E_a will result in a faster reaction rate under the same conditions. The E_a of hydrogen ab/desorption can be obtained using the Arrhenius equation (eqn (4)):

$$k(T) = Ae^{\frac{-E_a}{RT}}. (4)$$

That is eqn (5):

$$lnk(T) = -\frac{E_a}{RT} + lnA,$$
(5)

where k(T) is the rate constant and A is the pre-exponential factor.

The dissociation energy of $\rm H_2$ molecules is up to 432 kJ mol⁻¹ which acts as the initial rate-limiting step. Subsequently, the nucleation and growth of MgH₂ crystals are limited by the slow diffusion coefficient of H atoms in Mg ($\rm 10^{-13}~m^2~s^{-1}$); moreover, the firstly formed MgH₂ will act as an additional barrier due to the lower diffusion coefficient in MgH₂ ($\rm 10^{-16}~m^2~s^{-1}$), limiting further diffusion of H atoms to bulk Mg. The desorption of MgH₂ is mainly restricted by the high dissociation energy of Mg–H bonds ($\rm 160~kJ~mol^{-1}~H_2$) as well as the following diffusion of H escaping from MgH₂.

4.2 Mechanistic effects of core-shell nanostructured MgH₂ for hydrogen storage

mentioned construction of above, core-shell nanostructured MgH₂ is an effective approach to improve the thermodynamics and kinetics simultaneously. The catalytic shell with TM elements can accelerate the dissociation of H-H and Mg-H bonds, and the nanostructure stabilized by the shell can shorten the diffusion path of H atoms and increase the system energy by introducing extra interfaces. The details are discussed as follows.

4.2.1 Effect of catalysis. Transition metal (TM) groups have received significant attention since the 1990s owing to their excellent capabilities for hydrogen adsorption, dissociation, diffusion and recombination, which generally include transition metals and corresponding compounds. Liang et al. made MgH₂-TM (TM = 3d transition elements Ti, V, Mn, Fe, and Ni) nanocomposite powders by mechanical milling and studied the phase change during the absorption and desorption process systematically in 1999. 11 TiH2, VH0.81, Mg₂FeH₆, and Mg₂NiH₄ phase were found as catalysts in the Mg-Ti, Mg-V, Mg-Fe, and Mg-Ni composites, respectively, and Mn remained in the metallic state in the Mg-Mn case. Lu et al. investigated the structural changes during the dehydrogenation of the core-shell nanostructured Mg@Pt

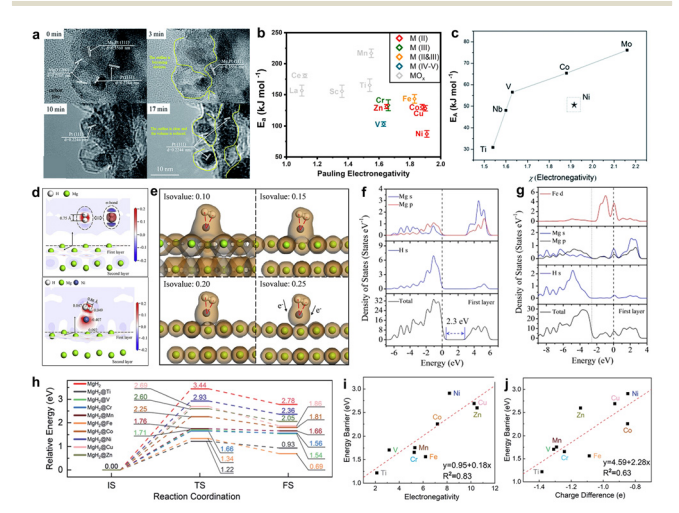


Fig. 6 (a) HRTEM images showing the microstructure evolution during the hydrogen desorption process induced by electron beam radiation in the hydrogenated Mg@Pt composite⁵⁹ (copyright 2019 Royal Society of Chemistry). (b and c) Scatter plot of active energy versus Pauling electronegativity of metal elements^{23,85} (copyright 2021 Elsevier, 2013 Royal Society of Chemistry). (d) Deformation charge density map of clean Mg(0001) with H₂ adsorption and Mg(0001) with Ni incorporation after H₂ adsorption. (e) Deformation charge density maps and charge density isosurface maps of Mg(0001) with Ni incorporation after H₂ adsorption⁸⁶ (copyright 2016 Elsevier). DOS of clean β -MgH₂(001) (f) and Fe-incorporated β -MgH₂(001) (g)⁸⁷ (copyright 2016 Elsevier). (h) Free energy profiles of MgH₂ dehydrogenation at MgH₂ and nine MgH₂/SAC-TM (TM = Ti, V, Cr, Mn, Fe, Co, Ni, Cu, and Zn) heterojunction systems, and correlations of (i) electronegativity vs. energy barrier, (j) metal charge difference vs. energy barrier83 (copyright 2022 Royal Society of Chemistry).

material by in situ high-resolution transmission electron microscopy (Fig. 6a).⁵⁸ They found that Pt nanoparticles in the shell had a "spillover" effect to enhance the initial absorption. In the continuous hydrogen hydrogen absorption, H-stabilized Mg₃Pt particles formed. During the hydrogen desorption process, the H atoms in Mg₃Pt left first, followed by H atoms/ions in MgH2 passing from MgH2 to Mg₃Pt, where Mg₃Pt acted as a "hydrogen pump" to accelerate the hydrogen desorption. The hydrogen storage mechanism of Mg-TM composites depends on the electron/ proton-transfer pathway during the ab/desorption process. The ability to lose or gain electrons of different TMs should be a key factor to influence the catalytic effect,82 and the electronegativity (χ) of a TM represents the ability to lose or gain an electron from a TM or TM ion. Huang et al. successfully synthesized a whole series of 3d transition elements (Sc, Ti, V, Cr, Mn, Fe, Co, Ni, Cu and Zn) and La and Ce transition metal catalysts highly dispersed on nitrogen-doped carbon (M-N-C).83 The correlation between the kinetics of MgH2-M-N-Cs and the electronegativity of M in M-N-Cs was confirmed. The M-N-Cs with high electronegativity center elements (V, Cr, Fe, Co, Ni, Cu, and Zn) showed a well-dispersed morphology and improved kinetics, whereas those with electronegativity lower than 1.6 (Sc, La, Ce, Ti, and Mn) showed unsatisfactory kinetic performance due to the oxidation and aggregation of metal atoms resulting from the strong affinity between these elements and oxygen. The estimated Ea of MgH2-M-N-C composites was in the descending order Ni < V < Cu < Co < Zn < Cr < Fe (Fig. 6b). Similarly, Cui et al. found that the activation energy for dehydrogenation (Ed) decreased with increasing electronegativity except for the Mg-Ni system (Fig. 6c).²³

In recent years, many researchers have further explained the effect of catalysts on Mg-based hydrogen storage through first-principles calculations. relationship between the microelectronic structure and the hydrogen storage properties has been elucidated, and experimental studies confirm the results of theoretical studies. Zhou et al. reported that the bond length of the H2 molecule absorbed on Ni-incorporated Mg(0001) had been extended to 0.86 Å compared with 0.75 Å on clean Mg(0001).84 A strong interaction existed between H2 and Ni and the electrons of H moved towards the Ni nucleus. The energy barrier of H2 dissociation had been significantly decreased and the diffusion became the limiting step with Ni incorporation (Fig. 6d). They also found that the incorporated Fe could act as a bridge that contributed to the electron transfer from the H anion to the Mg cation before H2 molecule formation (Fig. 6e).85 The calculated energy gap of β-MgH₂(001) was 2.3 eV, revealing their low electron mobility and strong ionic structure, while the energy gap between the valence band and the conduction band vanished with the hybridization of Mg s, Mg p, H s, and Fe d states (Fig. 6f and g). Dong et al. explicitly analyzed MgH2/singleatom catalyst (SAC) heterojunction systems including nine

different 3d transition metals (Ti, Cr, V, Mn, Fe, Co, Zn, Cu, and Ni) using spin-polarized DFTD3 calculations (Fig. 6h).86

The electronic properties of the single atom metal played an essential role in determining the dehydrogenation performance MgH₂/single-atom catalysts. of dehydrogenation energy barriers of MgH₂/single-atom catalysts showed good linear correlation with the electronegativity (Fig. 6i and j).

Metal compounds, such as oxides, carbides, halides, carbides, etc., can cover the Mg-based hydrogen storage materials to form core-shell structures, in addition to their catalytic effects on Mg-based hydrogen storage materials, and the by-products generated by the reaction of the metal compounds and magnesium during hydrogen absorption and desorption may further promote the hydrogen storage performance. Zhu et al. prepared Ni-doped Ti₃C₂ MXene catalyst (Ni@Ti-MX) and introduced it into MgH2 through ball milling. A synergetic effect of Mg2Ni, TiO2, Ti, and amorphous C derived in the MgH2 + Ni@Ti-MX composite exhibited remarkable improvements in the hydrogen sorption kinetics of MgH₂. 87 Such a unique core-shell structure makes different kinds of multivalent catalysts evenly distributed on the surface of Mg nanoparticles, and the Mg at the surface of the core can be fully in contact with the transition metal in the shell layer, which concurrently accelerates the hydrogen sorption rate.

4.2.2 Effect of active interfaces. All interfaces, especially solid-solid interfaces, are ubiquitous in nanoscale materials.88 The free energy change for the hydrogenation reaction of bulk Mg is given by eqn (6):

$$\ln \frac{p_{\text{H}_2,\text{bulk}}}{p_0} = \frac{\Delta_{\text{r}} G_{\text{bulk}}^0}{RT},$$
(6)

where $p_{H_0,bulk}$ is the pressure of hydrogen gas in equilibrium with Mg and MgH_2 phases at temperature T, and R is the gas constant. $\Delta_r G_{\text{bulk}}^0$ represents the Gibbs free energy of the Mg hydrogenation reaction under standard conditions (pressure p_0).

For nanosized Mg, the interface energy contribution to the Gibbs free energy has to be taken into account (the effect of the elastic strain is ignored) (eqn (7)):

$$\ln \frac{p_{\mathrm{H}_{2},\mathrm{nano}}}{p_{0}} = \frac{\Delta_{\mathrm{r}} G_{\mathrm{nano}}^{0}}{RT} \\
= \frac{1}{RT} \left[\Delta_{\mathrm{r}} G_{\mathrm{bulk}}^{0} + \sum_{i} (A\gamma)_{\mathrm{MgH}_{2}|i} - \sum_{i} (A\gamma)_{\mathrm{Mg}|i} \right], \quad (7)$$

where $p_{\rm H_2,nano}$ is the pressure of hydrogen gas in equilibrium with nanosized Mg and MgH2 phases, A is the interfacial area per mole Mg, and γ is the interface energy. $\Delta_r G_{nano}^0$ represents the Gibbs free energy of the Mg hydrogenation reaction under standard conditions (pressure p_0), and i represents catalytic component i (eqn (8)):

$$\ln \frac{p_{\rm H_2,nano}}{p_{\rm H_2,bulk}} = \frac{\sum_{i} (A\gamma)_{\rm MgH_2|i} - \sum_{i} (A\gamma)_{\rm Mg|i}}{RT}.$$
 (8)

Furthermore, we assume that the Mg/catalyst i interfaces remain well-defined after loading and unloading with hydrogen:

$$A_{\mathrm{MgH},|i} \approx A_{\mathrm{Mg}|i} \approx A$$

And with
$$\gamma_{\text{MgH}_2|i} - \gamma_{\text{Mg}|i} = \Delta \gamma$$
, (eqn (9)):

$$\ln \frac{p_{\text{H}_2,\text{nano}}}{p_{\text{H}_2,\text{bulk}}} = \frac{A\Delta \gamma}{RT}.$$
(9)

It is clear that a positive $\Delta \gamma$ results in a destabilization of the nanosized hydride phase with respect to the bulk hydride phase.

Dam et al. deposited two different multilayer stacks of Mg and Ti by magnetron sputtering, and the interface area changed with the thickness of Mg. 89 They observed different pressures indicating several thermodynamic equilibria, and the slope of the linear fit gave $\Delta \gamma = 0.35 \text{ J m}^{-2}$, which was in excellent agreement with calculations (Fig. 7a). Patelli et al. synthesized biphasic Mg-Ti-H nanoparticles that permitted complete absorption and desorption at a remarkably low temperature of 150 °C 7b).88 A model based on interface-induced (Fig. destabilization explaining the observed hydrogen sorption thermodynamics was established. The interface is conducive

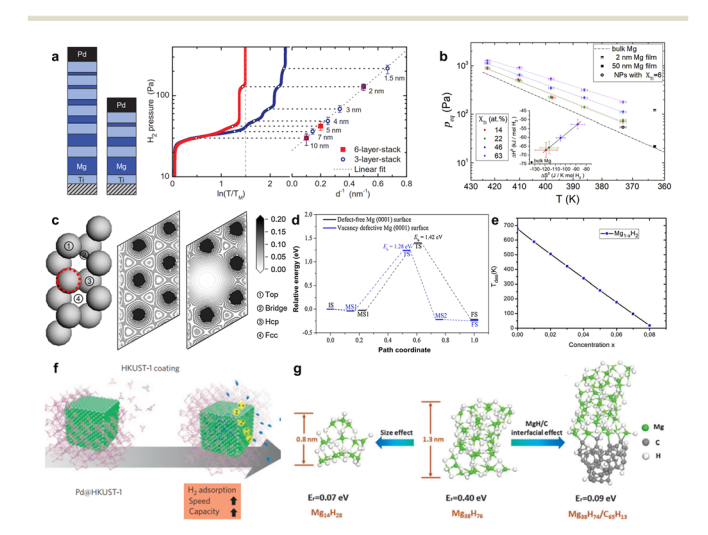


Fig. 7 (a) A schematic representation of the two Mg-Ti multilayer geometries and their absorption isotherms taken at 60 °C. From the equilibrium pressures versus the inverse thickness, the slope of the linear fit gives $\Delta \gamma = 0.35$ J m⁻²⁸⁹ (copyright 2011 Wiley-VCH). (b) Collection of all p_{eq} vs. T data for different X_{Ti} values⁸⁸ (copyright 2020 Elsevier). (c) Adsorption sites of H atom and charge density distribution of defect-free Mg(0001) surface and vacancy defective Mg(0001) surface; (d) corresponding calculated MEPs for H₂ molecule dissociation on defect-free and vacancy defective Mg(0001) surfaces⁹⁰ (copyright 2017 Elsevier). (e) Desorption temperature as a function of $V_{\rm Mq}$ concentration for Mg_{1-x}H₂ (ref. 91) (copyright 2020 Elsevier). (f) Schematic of the Pd@HKUST-1 (ref. 92) (copyright 2014 Springer Nature). (g) Reaction energy (E_r) for hydrogen release from clusters of pure $Mg_{14}H_{28}$ cluster, $Mg_{38}H_{76}$ cluster and $Mg_{38}H_{74}$ adsorbed on the cluster of amorphous carbon⁶⁸ (copyright 2013 Royal Society of

Mini review

to the generation of defect sites, and the defect sites can further improve the interface energy. Han *et al.* found that energy barriers of 1.42 eV require to be overcome for H₂ dissociation on defect-free surfaces and 1.28 eV for vacancy defective Mg(0001) surfaces, indicating that vacancy defects can moderately increase the reactivity of the Mg(0001) surface (Fig. 7c and d). Similarly, Bahou *et al.* reported that the desorption temperature decreased with increasing concentration of vacancy defects; however, the formation energy increased with increasing concentration of vacancy defects (Fig. 7e).

In addition, close interfacial contact facilitates charge transfer between the two phases, thus promoting the destabilization of the hydrogenated phase. Li et al. synthesized Pd nanocrystals covered with a metal-organic framework HKUST-1 (Fig. 7f).92 The XPS spectra of Pd@HKUST-1 suggested that the electrons in the Pd nanocubes were slightly transferred to the HKUST-1 shell, which might be responsible for the increased number of holes in the 4d band of Pd nanocubes with the HKUST-1 coating, resulting in the enhanced hydrogen storage capacity. Jia et al. studied the interfacial effect between nanoconfined Mg/MgH2 and carbon, which originated from the charge transfer between the supported surface and the reactants.⁶⁸ Mg-C bonding did transfer electrons from MgH₂ nanoparticles to the CMK-3 substrate; as a consequence, the Mg-H bonding had been weakened. The reaction energies for hydrogen release from clusters of Mg38H76 cluster and Mg38H74 adsorbed on the cluster of amorphous carbon were determined to be 0.40 eV and 0.09 eV, respectively (Fig. 7g). The thermodynamic stability of the Mg-H system could also be drastically modified by elastic constraints raised as a consequence of alloying between Mg and the catalytic layer. 93 In summary, the core-shell structure can greatly increase the interface area, and the core-shell junction is the favorable position for defects. Therefore, the system energy can be improved by additional interface, which is conducive to the completion of hydrogen absorption and desorption at a lower temperature for Mg-based hydrogen storage materials.

4.2.3 Effect of nanoconfinement. Many recent experiments and theoretical calculations have suggested that nanostructured metal hydrides have significantly different thermodynamic and kinetic performance than their bulk counterparts. As mentioned in the previous section, more atoms are exposed at the surface for nanoscale materials, which leads to an increase in surface energy. By considering these additional surface factors, we obtain the van't Hoff equation (eqn (10)):

$$\ln \frac{p_{\text{H}_2,\text{nano}}}{p_0} = \frac{\Delta_{\text{r}} G_{\text{nano}}^0}{RT}
= \frac{1}{RT} \left[\Delta_{\text{r}} H^0 + \left(\frac{3V_{\text{MgH}_2} \gamma_{\text{MgH}_2}}{r_{\text{MgH}_2}} - \frac{3V_{\text{Mg}} \gamma_{\text{Mg}}}{r_{\text{Mg}}} \right) \right] - \frac{\Delta S^0}{R}.$$
(10)

Part of the heat of formation will be stored as excess surface energy during the hydrogen absorption, which will result in a

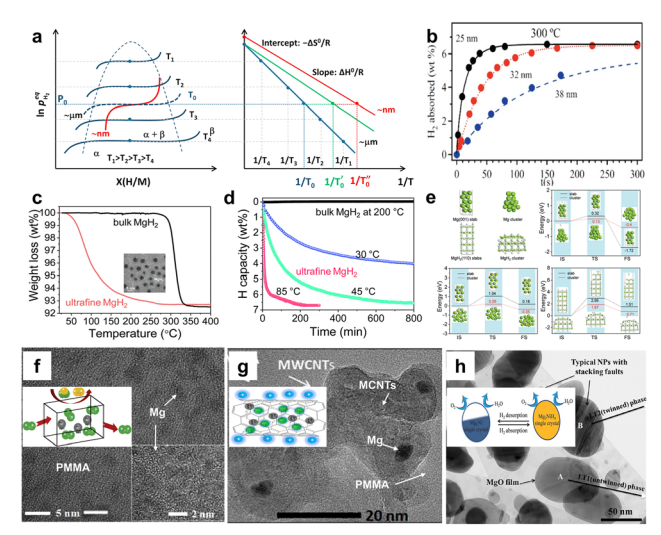


Fig. 8 (a) PCT profiles and the corresponding van't Hoff plots of MgH $_2$ systems (copyright 2017, Elsevier). (b) Hydrogen absorption of the different sized Mg nanocrystal samples at 300 $^{\circ}\text{C}^{96}$ (copyright 2011 American Chemical Society). (c) TGA isothermal and (d) under different conditions of bulk and non-confined ultrafine MgH $_2$. (e) Computational models of hydrogen uptake, diffusion and release steps for bulk and nanosized Mg and MgH $_2$ (copyright 2021 Royal Society of Chemistry). (f) HR-TEM image of PMMA/MgH $_2$ composite (inset: hydrogen sorption cycling schematic) (copyright 2019 Elsevier). (g) HR-TEM image of PMMA/MCNTs/MgH $_2$ composite (inset: Mg nanoparticles supported by a selectively gas-permeable matrix) (copyright 2019 Elsevier). (h) Bright-field TEM image of Mg $_2$ NiH $_4$ nanoparticles covered by MgO (inset: detailed description process of a single microencapsulated particle) (copyright 2019 Wiley-VCH).

lower enthalpy; correspondingly, the plateau pressure at the same temperature will increase. The influence of surface energy on the enthalpy change increases with the decrease of particle size (Fig. 8a).

Wagemans et al. systematically investigated the effect of crystal grain size on the thermodynamic stability of magnesium and magnesium hydride, using ab initio Hartree-Fock and density functional theory calculations. 95 The hydrogen desorption energy decreased significantly when the crystal grain size became smaller than ~1.3 nm. The MgH₂ crystallite size of 0.9 nm corresponded to a desorption temperature of only 200 °C. Norberg et al. synthesized Mg nanocrystals of 25, 32, and 38 nm controllable sizes and the small particles absorbed more hydrogen at the same time and temperature (Fig. 8b).96 Zhang et al. developed a novel strategy to synthesize nanoscale MgH2 with the assistance of ultrasound. 97 The ultrafine MgH2 with the size of 4-5 nm started to release hydrogen at 30 °C (Fig. 8c and d), and calculations revealed that the reaction barrier of H2 disassociation, diffusion, and release for Mg cluster was lower than that on the Mg(001) slab (Fig. 8e). On the whole, it is difficult to synthesize free-standing ultrafine MgH2 nanoparticles (<10 nm) due to their high surface energy, strong reduction trend, and high water-oxygen sensitivity. Confining Mg/MgH2 nanoparticles into porous scaffold materials, i.e., protected by an inert shell, can prohibit

agglomeration and grain growth, which are stable over many hydrogen release and uptake cycles. 6,50,98 Konarova et al. synthesized MgH₂/CMK-3 compounds with 20 wt% loading that released hydrogen at a temperature of 253 °C, and its corresponding decomposition enthalpy was equal to 52.38 kJ mol⁻¹ H₂. ⁹⁹ Nielsen et al. found that the size of MgH₂ nanoparticle embedded in nanoporous carbon aerogel was related with the pore size distribution of the scaffold, and the smaller pores mediated faster desorption rate.⁶⁸ Liang et al. prepared air-stable Mg nanoparticles in situ reduced in PMMA and PMMA/MCNTs (Fig. 8f and g). 100,101 The PMMA shell could be permeated with H2, but O2 and H2O molecules could not infiltrate, and the porous structure of the MWCNT-PMMA served as hydrogen diffusion channels. The composite samples exhibit improved hydrogen storage properties and stable uptake/release cycles. Zhang et al. synthesized monodispersed Mg2NiH4 single-crystal nanoparticles that were encapsulated in situ into a well-defined ultrathin MgO layer (Fig. 8h).²⁸ The MgO layer had superior gas-selective permeability to prevent air poisoning while being accessible for hydrogen to pass through. On the whole, nanoscale Mg possesses significantly better hydrogen storage performances than bulk Mg, and the shell covering on the surface of nanoparticles can effectively inhibit the agglomeration of nanoparticles in the thermally induced process of hydrogen absorption and desorption. Meanwhile, other characteristics of the shell structure, such as gas-selective permeability, can render the nanoconfined composites with distinct properties.

5 The promising applications of coreshell nanostructured magnesiumbased hydrogen storage materials

Core-shell nanostructured Mg-based hydrogen storage materials show excellent hydrogen absorption and desorption kinetics and long-term cycling performances. Such a unique structure renders the composites some outstanding

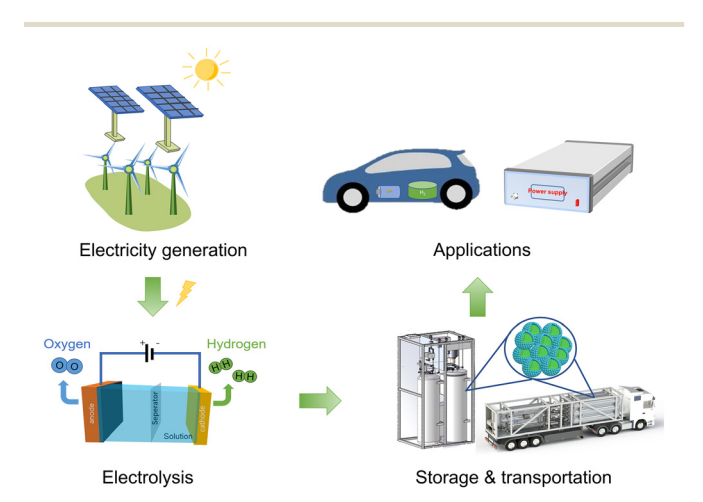


Fig. 9 A vision of the future applications of core-shell nanostructured Mg-based hydrogen storage materials.

properties, for example, anti-air oxidation ability, rapid hydrolysis rate, etc. Considering the above, we suggest a bright vision for the use of core-shell nanostructured Mgbased hydrogen storage materials in the future (Fig. 9). Environmentally friendly hydrogen can be obtained by electrolysis of water using electricity generated from renewable sources, such as solar energy and wind energy, and the hydrogen is reserved in a solid Mg-based hydrogen storage tank. Core-shell nanostructured Mg-based materials can absorb and desorb hydrogen at a relatively low temperature, which significantly reduces the energy consumption during hydrogen storage. Moreover, core-shell nanostructured Mg-based materials have the advantages of excellent reversibility under the protection of their shell structures, which is available for commercial applications. In addition, core-shell nanostructured Mg-based materials exhibit outstanding hydrolysis performances. During the hydrolysis process of pure Mg particles, a magnesium hydroxide film will be formed on the surface, thereby inhibiting the progress of the hydrolysis reaction. 102 The shell components of core-shell nanostructured Mg-based composites can effectively prevent the formation of dense magnesium hydroxide film on the surface. Meanwhile, some materials generated in the shell through reaction with water can serve as catalysts to regulate the hydrolysis rate of MgH₂. 47,103 The storage system, producing hydrogen by pyrolysis or hydrolysis, could supply hydrogen source to a fuel cell for electricity generation, small-scale portable emergency power supply, industry usage, and so on. Indeed, core-shell nanostructured Mg-based hydrogen storage materials will play an important role in future hydrogen energy systems.

6 Summary and outlook

MgH₂/Mg-based hydrogen storage systems have attracted much attention for possible applications as promising hydrogen carriers due to their high hydrogen storage density, good cycling performance, and high abundance of Mg on earth. However, the high hydrogen desorption temperature and slow absorption and desorption rate impede its practical applications. Adding catalysts is one of the most effective methods to reduce the dehydrogenation temperature of Mgbased hydrogen storage materials, and the optimization of catalysts is thus highly important. In addition, only when the size of magnesium hydride particles is reduced down to a certain extent can the modification in both thermodynamics and kinetics be achieved. It is clear from the discussion above that the development of core-shell nanostructured Mgbased hydrogen storage materials has provided an effective solution for simultaneously improving the thermodynamic and kinetic properties of Mg-based materials. Many experimental and theoretical investigations have shown the relationships between core-shell structures and improved hydrogen sorption properties of Mg/MgH2. Meanwhile, it is

necessary to develop new design principles for such specific structured hydrogen storage materials in the future.

In this review, we have presented inspiring research progress in the field of core-shell nanostructured magnesium-based hydrogen storage materials, mainly focusing on the preparation methods, microstructures, properties and related mechanisms. Various methods were developed to regulate the core-shell structures of Mg-based hydrogen storage materials from nanoscale. Ball milling and arc plasma methods are physical strategies, while electroless plating and nanoconfinement methods belong to chemical ones. Ball milling is easy to operate but with high energy consumption and long duration. The arc plasma method is highly controllable and suitable for industrial production. The electroless plating method is sensitive to experimental conditions, including the composition, stirring rate, the kinds of reactants and so on, but it is usable to explore optimized core-shell nanostructures in the lab because of the compatibility. Nanoconfinement of Mg/MgH₂ nanoparticles in porous scaffolds exhibits outstanding hydrogen storage performance where the scaffolds lower the total hydrogen storage capacity of the system. It is especially important to find the optimal processing parameters and technical routes to synthesize advanced core-shell nanostructured Mg/MgH2 nanoparticles with smaller size and better catalytic shell for improving their hydrogen storage properties and balance the benefits and costs. It is recognized that through efficiently combining the size effect of the Mg core and the catalytic effect of the shell, significantly improved thermodynamic, kinetic and cycling performances can be achieved in order to meet the requirements for industrial applications.

Conflicts of interest

There are no conflicts to declare.

Acknowledgements

The authors would like to acknowledge the support from the National Key Research & Development Program (2022YFB3803700) of China and the National Natural Science Foundation (No. 52171186). We also appreciate the support from the Center of Hydrogen Science, Shanghai Jiao Tong University.

References

- 1 R. B. Jackson, C. Le Quéré, R. M. Andrew, J. G. Canadell, G. P. Peters, J. Roy and L. Wu, Warning signs for stabilizing global CO₂ emissions, *Environ. Res. Lett.*, 2017, 12, 110202.
- 2 M. D. Allendorf, V. Stavila, J. L. Snider, M. Witman, M. E. Bowden, K. Brooks, B. L. Tran and T. Autrey, Challenges to developing materials for the transport and storage of hydrogen, *Nat. Chem.*, 2022, 14, 1214–1223.
- 3 J. O. Abe, A. P. I. Popoola, E. Ajenifuja and O. M. Popoola, Hydrogen energy, economy and storage: Review and

- recommendation, Int. J. Hydrogen Energy, 2019, 44, 15072-15086.
- 4 A. W. C. van den Berg and C. O. Areán, Materials for hydrogen storage: current research trends and perspectives, *Chem. Commun.*, 2008, 668–681.
- 5 F. Zhang, P. Zhao, M. Niu and J. Maddy, The survey of key technologies in hydrogen energy storage, *Int. J. Hydrogen Energy*, 2016, 41, 14535–14552.
- 6 A. Schneemann, J. L. White, S. Kang, S. Jeong, L. F. Wan, E. S. Cho, T. W. Heo, D. Prendergast, J. J. Urban, B. C. Wood, M. D. Allendorf and V. Stavila, Nanostructured metal hydrides for hydrogen storage, *Chem. Rev.*, 2018, 118, 10775–10839.
- 7 Target explanation document: Onboard hydrogen storage for light-duty fuel cell vehicles, United States Department of Energy, Washington, DC, 2017, https://www.energy.gov/ eere/fuelcells/articles/target-explanation-document-onboardhydrogen-storage-light-duty-fuel-cell.
- 8 Y. Sun, C. Shen, Q. Lai, W. Liu, D. W. Wang and K. F. Aguey-Zinsou, Tailoring magnesium based materials for hydrogen storage through synthesis: Current state of the art, *Energy Storage Mater.*, 2018, **10**, 168–198.
- 9 J. F. Stampfer Jr., C. E. Holley Jr. and J. F. Suttle, The magnesium-Hydrogen System, *J. Am. Chem. Soc.*, 1960, **82**, 3504–3508.
- 10 G. Barkhordarian, T. Klassen and R. Bormann, Fast hydrogen sorption kinetics of nanocrystalline Mg using Nb₂O₅ as catalyst, Scr. Mater., 2003, 49, 213–217.
- 11 G. Liang, J. Huot, S. Boily, A. Van Neste and R. Schulz, Catalytic effect of transition metals on hydrogen sorption in nanocrystalline ball milled MgH₂-Tm (Tm=Ti, V, Mn, Fe and Ni) systems, *J. Alloys Compd.*, 1999, 292, 247–252.
- 12 T. Liu, C. Chen, F. Wang and X. Li, Enhanced hydrogen storage properties of magnesium by the synergic catalytic effect of TiH_{1.971} and TiH_{1.5} nanoparticles at room temperature, *J. Power Sources*, 2014, **267**, 69–77.
- 13 P. M. Jardim, M. O. T. da Conceição, M. C. Brum and D. S. dos Santos, Hydrogen sorption kinetics of ball-milled MgH₂-TiO₂ based 1D nanomaterials with different morphologies, *Int. J. Hydrogen Energy*, 2015, 40, 17110–17117.
- 14 J. Chen, G. Xia, Z. Guo, Z. Huang, H. Liu and X. Yu, Porous Ni nanofibers with enhanced catalytic effect on the hydrogen storage performance of MgH₂, *J. Mater. Chem. A*, 2015, 3, 15843–15848.
- 15 J. J. Reilly and R. H. Wiswall, Reaction of hydrogen with alloys of magnesium and nickel and the formation of Mg₂NiH₄, *Inorg. Chem.*, 1968, 7, 2254–2256.
- 16 K. Edalati, R. Uehiro, Y. Ikeda, H. W. Li, H. Emami, Y. Filinchuk, M. Arita, X. Sauvage, I. Tanaka, E. Akiba and Z. Horita, Design and synthesis of a magnesium alloy for room temperature hydrogen storage, *Acta Mater.*, 2018, 149, 88–96.
- 17 W. Li, C. Li, H. Ma and J. Chen, Magnesium nanowires: Enhanced kinetics for hydrogen absorption and desorption, *J. Am. Chem. Soc.*, 2007, **129**, 6710–6711.

- 18 H. Shao, G. Xin, J. Zheng, X. Li and E. Akiba, Nanotechnology in Mg-based materials for hydrogen storage, Nano Energy, 2012, 1, 590-601.
- 19 G. Xia, Y. Tan, X. Chen, D. Sun, Z. Guo, H. Liu, L. Ouyang, M. Zhu and X. Yu, Monodisperse magnesium hydride nanoparticles uniformly self-assembled on graphene, Adv. Mater., 2015, 27, 5981-5988.
- 20 W. Zhu, L. Ren, C. Lu, H. Xu, F. Sun, Z. Ma and J. Zou, Nanoconfined and in situ catalyzed MgH2 self-assembled on 3D Ti₃C₂ MXene folded nanosheets with enhanced hydrogen sorption performances, ACS Nano, 2021, 15, 18494-18504.
- 21 L. Pasquini, M. Sacchi, M. Brighi, C. Boelsma, S. Bals, T. Perkisas and B. Dam, Hydride destabilization in core-shell nanoparticles, Int. J. Hydrogen Energy, 2014, 39, 2115-2123.
- 22 J. Cui, H. Wang, J. Liu, L. Ouyang, Q. Zhang, D. Sun, X. Yao and M. Zhu, Remarkable enhancement in dehydrogenation of MgH2 by a nano-coating of multi-valence Ti-based catalysts, I. Mater. Chem. A, 2013, 1, 5603-5611.
- 23 J. Cui, J. Liu, H. Wang, L. Ouyang, D. Sun, M. Zhu and X. Yao, Mg-TM (TM: Ti, Nb, V, Co, Mo or Ni) core-shell like nanostructures: synthesis, hydrogen storage performance and catalytic mechanism, J. Mater. Chem. A, 2014, 2, 9645-9655.
- 24 X. Xie, C. Hou, C. Chen, X. Sun, Y. Pang, Y. Zhang, R. Yu, B. Wang and W. Du, First-principles studies in Mg-based hydrogen storage Materials: A review, Energy, 2020, 211, 118959.
- 25 S. Banerjee, C. G. S. Pillai and C. Majumder, Dissociation and diffusion of hydrogen on the Mg (0001) surface: Catalytic effect of V and Ni double substitution, J. Phys. Chem. C, 2009, 113, 10574-10579.
- 26 Z. Y. Wang and Y. J. Zhao, Role of metal impurity in hydrogen diffusion from surface into bulk magnesium: theoretical study, Phys. Lett. 3696-3700.
- 27 H. C. Wang, D. H. Wu, L. T. Wei and B. Y. Tang, Firstprinciples investigation of dehydrogenation on Cu-doped MgH₂ (001) and (110) surfaces, J. Phys. Chem. C, 2014, 118, 13607-13616
- 28 J. Zhang, Y. Zhu, H. Lin, Y. Liu, Y. Zhang, S. Li, Z. Ma and L. Li, Metal hydride nanoparticles with ultrahigh structural stability and hydrogen storage activity derived from microencapsulated nanoconfinement, Adv. Mater., 2017, 29, 1700760.
- 29 K. Wang, X. Zhang, Z. Ren, X. Zhang, J. Hu, M. Gao, H. Pan and Y. Liu, Nitrogen-stimulated superior catalytic activity of niobium oxide for fast full hydrogenation of magnesium at ambient temperature, Energy Storage Mater., 2019, 23, 79-87.
- 30 M. Liu, X. Xiao, S. Zhao, M. Chen, J. Mao, B. Luo and L. Chen, Facile synthesis of Co/Pd supported by few-walled carbon nanotubes as an efficient bidirectional catalyst for improving the low temperature hydrogen storage properties of magnesium hydride, J. Mater. Chem. A, 2019, 7, 5277-5287.

- 31 X. Lu, L. Zhang, H. Yu, Z. Lu, J. He, J. Zheng, F. Wu and L. Chen, Achieving superior hydrogen storage properties of MgH₂ by the effect of TiFe and carbon nanotubes, Chem. Eng. J., 2021, 422, 130101.
- 32 K. Xian, M. Wu, M. Gao, S. Wang, Z. Li, P. Gao, Z. Yao, Y. Liu, W. Sun and H. Pan, A unique nanoflake-shape bimetallic Ti-Nb oxide of superior catalytic effect for hydrogen storage of MgH₂, Small, 2022, 18, 2107013.
- 33 S. El-Eskandarany, Mechanical alloying, second edition: nanotechnology, materials science and powder metallurgy, Elsevier, 2015.
- 34 M. S. El-Eskandarany, Recent developments in the fabrication, characterization and implementation of MgH2based solid-hydrogen materials in the Kuwait Institute for Scientific Research, RSC Adv., 2019, 9, 9907-9930.
- 35 J. Liu, Y. Liu, Z. Liu, Z. Ma, Y. Ding, Y. Zhu, Y. Zhang, J. Zhang and L. Li, Effect of rGO supported NiCu derived from layered double hydroxide on hydrogen sorption kinetics of MgH₂, I. Alloys Compd., 2019, 789, 768-776.
- 36 M. Anik, I. Akay and S. Topcu, Effect of electroless nickel coating on the electrochemical hydrogen storage characteristics of Al and Zr including Mg-based alloys, Int. J. Hydrogen Energy, 2009, 34, 5449-5457.
- 37 C. Lu, J. Zou, X. Shi, X. Zeng and W. Ding, Synthesis and hydrogen storage properties of core-shell structured binary Mg@Ti and ternary Mg@Ti@Ni composites, Int. J. Hydrogen Energy, 2017, 42, 2239-2247.
- 38 C. Lu, J. Zou, X. Zeng and W. Ding, Hydrogen storage properties of core-shell structured Mg@TM (TM = Co, V) composites, Int. J. Hydrogen Energy, 2017, 42, 15246-15255.
- 39 W. Liu and K. F. Aguey-Zinsou, Hydrogen storage properties of in-situ stabilised magnesium nanoparticles generated by electroless reduction with alkali metals, Int. J. Hydrogen Energy, 2015, 40, 16948-16960.
- 40 T. Liu, Y. Zhang and X. Li, Preparations and characteristics of Ti hydride and Mg ultrafine particles by hydrogen plasma-metal reaction, Scr. Mater., 2003, 48, 397-402.
- 41 H. Shao, Y. Wang, H. Xu and X. Li, Hydrogen storage properties of magnesium ultrafine particles prepared by hydrogen plasma-metal reaction, Mater. Sci. Eng., B, 2004, 110, 221-226.
- 42 J. Zou, X. Zeng, Y. Ying, P. Stephane and W. Ding, Preparation and hydrogen sorption properties of a nanostructured Mg based Mg-La-O composite, Int. J. Hydrogen Energy, 2012, 37, 13067-13073.
- 43 J. Zou, X. Zeng, Y. Ying, X. Chen, H. Guo, S. Zhou and W. Ding, Study on the hydrogen storage properties of coreshell structured Mg-RE (RE = Nd, Gd, Er) nano-composites synthesized through arc plasma method, Int. J. Hydrogen Energy, 2013, 38, 2337-2346.
- 44 S. Long, J. Zou, X. Chen, X. Zeng and W. Ding, A comparison study of Mg-Y2O3 and Mg-Y hydrogen storage composite powders prepared through arc plasma method, J. Alloys Compd., 2014, 615, S684-S688.
- 45 J. Mao, J. Zou, C. Lu, X. Zeng and W. Ding, Hydrogen storage and hydrolysis properties of core-shell structured

- Mg-MF_x (M=V, Ni, La and Ce) nano-composites prepared by arc plasma method, *J. Power Sources*, 2017, **366**, 131–142.
- 46 Y. C. Pan, J. X. Zou, X. Q. Zeng and W. J. Ding, Hydrogen storage properties of Mg-TiO₂ composite powder prepared by arc plasma method, *Trans. Nonferrous Met. Soc. China*, 2014, 24, 3834–3839.
- 47 B. Yang, J. Zou, T. Huang, J. Mao, X. Zeng and W. Ding, Enhanced hydrogenation and hydrolysis properties of coreshell structured $Mg\text{-}MO_x$ (M = Al, Ti and Fe) nanocomposites prepared by arc plasma method, *Chem. Eng. J.*, 2019, 371, 233–243.
- 48 X. Xie, M. Chen, P. Liu, J. Shang and T. Liu, Synergistic catalytic effects of the Ni and V nanoparticles on the hydrogen storage properties of Mg-Ni-V nanocomposite, *Chem. Eng. J.*, 2018, 347, 145–155.
- 49 J. Zou, H. Sun, X. Zeng, G. Ji and W. Ding, Preparation and hydrogen storage properties of Mg-rich Mg-Ni ultrafine particles, *J. Nanomater.*, 2012, 2012, 592147.
- 50 X. Yu, Z. Tang, D. Sun, L. Ouyang and M. Zhu, Recent advances and remaining challenges of nanostructured materials for hydrogen storage applications, *Prog. Mater. Sci.*, 2017, **88**, 1–48.
- 51 M. Paskevicius, H. Y. Tian, D. A. Sheppard, C. J. Webb, M. P. Pitt, E. M. Gray, N. M. Kirby and C. E. Buckley, Magnesium hydride formation within carbon aerogel, J. Phys. Chem. C, 2011, 115, 1757–1766.
- 52 Y. Liu, J. Zou, X. Zeng, X. Wu, H. Tian, W. Ding, J. Wang and A. Walter, Study on hydrogen storage properties of Mg nanoparticles confined in carbon aerogels, *Int. J. Hydrogen Energy*, 2013, 38, 5302–5308.
- 53 Z. Zhao-Karger, J. Hu, A. Roth, D. Wang, C. Kübel, W. Lohstroh and M. Fichtner, Altered thermodynamic and kinetic properties of MgH₂ infiltrated in microporous scaffold, *Chem. Commun.*, 2010, 46, 8353–8355.
- 54 L. Ren, W. Zhu, Q. Zhang, C. Lu, F. Sun, X. Lin and J. Zou, MgH₂ confinement in MOF-derived N-doped porous carbon nanofibers for enhanced hydrogen storage, *Chem. Eng. J.*, 2022, 434, 134701.
- 55 Y. Wang and Y. Wang, Recent advances in additiveenhanced magnesium hydride for hydrogen storage, *Prog. Nat. Sci.: Mater. Int.*, 2017, 27, 41–49.
- 56 Y. J. Choi, J. W. Choi, H. Y. Sohn, T. Ryu, K. S. Hwang and Z. Z. Fang, Chemical vapor synthesis of Mg-Ti nanopowder mixture as a hydrogen storage material, *Int. J. Hydrogen Energy*, 2009, 34, 7700–7706.
- 57 N. Hanada, T. Ichikawa and H. Fujii, Catalytic effect of nanoparticle 3d-transition metals on hydrogen storage properties in magnesium hydride MgH₂ prepared by mechanical milling, *J. Phys. Chem. B*, 2005, **109**, 7188–7194.
- 58 J. Zou, S. Long, L. Zhang, C. Lu, X. Chen, X. Zeng and W. Ding, Hydrogen sorption behaviors of a core-shell Structured Mg@Fe composite powder, *Mater. Trans.*, 2014, 55, 1156–1160.
- 59 C. Lu, Y. Ma, F. Li, H. Zhu, X. Zeng, W. Ding, T. Deng, J. Wu and J. Zou, Visualization of fast "hydrogen pump" in

- core-shell nanostructured Mg@Pt through hydrogen-stabilized Mg₃Pt, *J. Mater. Chem. A*, 2019, 7, 14629–14637.
- 60 H. J. Lin, J. J. Tang, Q. Yu, H. Wang, L. Z. Ouyang, Y. J. Zhao, J. W. Liu, W. H. Wang and M. Zhu, Symbiotic CeH_{2.73}/CeO₂ catalyst: A novel hydrogen pump, *Nano Energy*, 2014, 9, 80–87.
- 61 M. Chen, X. Xiao, X. Wang, Y. Lu, M. Zhang, J. Zheng and L. Chen, Self-templated carbon enhancing catalytic effect of ZrO₂ nanoparticles on the excellent dehydrogenation kinetics of MgH₂, Carbon, 2020, 166, 46–55.
- 62 Z. Wang, Z. Ren, N. Jian, M. Gao, J. Hu, F. Du, H. Pan and Y. Liu, Vanadium oxide nanoparticles supported on cubic carbon nanoboxes as highly active catalyst precursors for hydrogen storage in MgH₂, *J. Mater. Chem. A*, 2018, 6, 16177–16185.
- 63 J. Zou, H. Guo, X. Zeng, S. Zhou, X. Chen and W. Ding, Hydrogen storage properties of Mg-TM-La (TM = Ti, Fe, Ni) ternary composite powders prepared through arc plasma method, *Int. J. Hydrogen Energy*, 2013, **38**, 8852–8862.
- 64 S. U. Rather, A. A. Taimoor, A. Muhammad, Y. A. Alhamed, S. F. Zaman and A. M. Ali, Kinetics of hydrogen adsorption on MgH₂/CNT composite, *Mater. Res. Bull.*, 2016, 77, 23–28.
- 65 M. A. Lillo-Ródenas, Z. X. Guo, K. F. Aguey-Zinsou, D. Cazorla-Amorós and A. Linares-Solano, Effects of different carbon materials on MgH₂ decomposition, *Carbon*, 2008, 46, 126–137.
- 66 K. J. Jeon, H. R. Moon, A. M. Ruminski, B. Jiang, C. Kisielowski, R. Bardhan and J. J. Urban, Air-stable magnesium nanocomposites provide rapid and high-capacity hydrogen storage without using heavy-metal catalysts, *Nat. Mater.*, 2011, 10, 286–290.
- 67 E. S. Cho, A. M. Ruminski, S. Aloni, Y. S. Liu, J. Guo and J. J. Urban, Graphene oxide/metal nanocrystal multilaminates as the atomic limit for safe and selective hydrogen storage, *Nat. Commun.*, 2016, 7, 10804.
- 68 Y. Jia, C. Sun, L. Cheng, M. Abdul Wahab, J. Cui, J. Zou, M. Zhu and X. Yao, Destabilization of Mg-H bonding through nano-interfacial confinement by unsaturated carbon for hydrogen desorption from MgH₂, *Phys. Chem. Chem. Phys.*, 2013, 15, 5814–5820.
- 69 T. K. Nielsen, K. Manickam, M. Hirscher, F. Besenbacher and T. R. Jensen, Confinement of MgH₂ nanoclusters within nanoporous aerogel scaffold materials, ACS Nano, 2009, 3, 3521–3528.
- 70 C. Zlotea, C. Chevalier-César, E. Léonel, E. Leroy, F. Cuevas, P. Dibandjo, C. Vix-Guterl, T. Martens and M. Latroche, Synthesis of small metallic Mg-based nanoparticles confined in porous carbon materials for hydrogen sorption, *Faraday Discuss.*, 2011, 151, 117–131.
- 71 M. Hu, X. Xie, M. Chen, C. Zhu and T. Liu, TiC_X-decorated Mg nanoparticles confined in carbon shell: Preparation and catalytic mechanism for hydrogen storage, *J. Alloys Compd.*, 2020, 817, 152813.
- 72 D. W. Lim, J. W. Yoon, K. Y. Ryu and M. P. Suh, Magnesium nanocrystals embedded in a metal-organic framework: hybrid hydrogen storage with synergistic effect on physi-

- and chemisorption, *Angew. Chem., Int. Ed.*, 2012, **51**, 9814–9817.
- 73 S. Gadipelli, J. Ford, W. Zhou, H. Wu, T. J. Udovic and T. Yildirim, Nanoconfinement and catalytic dehydrogenation of ammonia borane by magnesium-metal-organic-framework-74, *Chem. Eur. J.*, 2011, 17, 6043–6047.
- 74 Z. Ma, Q. Zhang, S. Panda, W. Zhu, F. Sun, D. Khan, J. Dong, W. Ding and J. Zou, In situ catalyzed and nanoconfined magnesium hydride nanocrystals in a Ni-MOF scaffold for hydrogen storage, *Sustainable Energy Fuels*, 2020, 4, 4694–4703.
- 75 Z. Ma, S. Panda, Q. Zhang, F. Sun, D. Khan, W. Ding and J. Zou, Improving hydrogen sorption performances of MgH₂ through nanoconfinement in a mesoporous CoS nanoboxes scaffold, *Chem. Eng. J.*, 2021, 406, 126790.
- 76 Z. Sun, X. Lu, F. M. Nyahuma, N. Yan, J. Xiao, S. Su and L. Zhang, Enhancing hydrogen storage properties of MgH₂ by transition metals and carbon materials: A brief review, Front. Chem., 2020, 8, 1–14.
- 77 M. Lotoskyy, R. Denys, V. A. Yartys, J. Eriksen, J. Goh, S. N. Nyamsi, C. Sita and F. Cummings, An outstanding effect of graphite in nano-MgH₂-TiH₂ on hydrogen storage performance, *J. Mater. Chem. A*, 2018, 6, 10740–10754.
- 78 M. Chen, M. Hu, X. Xie and T. Liu, High loading nanoconfinement of V-decorated Mg with 1 nm carbon shells: hydrogen storage properties and catalytic mechanism, *Nanoscale*, 2019, 11, 10045–10055.
- 79 X. Xie, M. Chen, M. Hu, B. Wang, R. Yu and T. Liu, Recent advances in magnesium-based hydrogen storage materials with multiple catalysts, *Int. J. Hydrogen Energy*, 2019, 44, 10694–10712.
- 80 R. Bardhan, A. M. Ruminski, A. Brand and J. J. Urban, Magnesium nanocrystal-polymer composites: A new platform for designer hydrogen storage materials, *Energy Environ. Sci.*, 2011, 4, 4882–4895.
- 81 K. F. Aguey-Zinsou and J. R. Ares-Fernández, Hydrogen in magnesium: new perspectives toward functional stores, *Energy Environ. Sci.*, 2010, 3, 526–543.
- 82 J. Lyu, V. Kudiiarov, L. Svyatkin, A. Lider and K. Dai, On the Catalytic Mechanism of 3d and 4d transition-metal-based materials on the hydrogen sorption properties of Mg/MgH₂, Catalysts, 2023, 13, 519.
- 83 Y. Huang, C. An, Q. Zhang, L. Zang, H. Shao, Y. Liu, Y. Zhang, H. Yuan, C. Wang and Y. Wang, Cost-effective mechanochemical synthesis of highly dispersed supported transition metal catalysts for hydrogen storage, *Nano Energy*, 2021, 80, 105535.
- 84 B. Liu, B. Zhang, Y. Wu, W. Lv and S. Zhou, Theoretical prediction and experimental study on catalytic mechanism of incorporated Ni for hydrogen absorption of Mg, *Int. J. Hydrogen Energy*, 2019, 44, 27885–27895.
- 85 H. Chen, H. Yu, Q. Zhang, B. Liu, P. Liu, X. Zhou, Z. Han and S. Zhou, Enhancement in dehydriding performance of magnesium hydride by iron incorporation: A combined experimental and theoretical investigation, *J. Power Sources*, 2016, 322, 179–186.

- 86 S. Dong, C. Li, E. Lv, J. Wang, H. Liu, Z. Gao, W. Xiong, Z. Ding, W. Yang and H. Li, MgH₂/single-atom heterojunctions: effective hydrogen storage materials with facile dehydrogenation, *J. Mater. Chem. A*, 2022, 10, 19839–19851.
- 87 W. Zhu, S. Panda, C. Lu, Z. Ma, D. Khan, J. Dong, F. Sun, H. Xu, Q. Zhang and J. Zou, Using a self-assembled two-dimensional MXene-based catalyst (2D-Ni@Ti₃C₂) to enhance hydrogen storage properties of MgH₂, *ACS Appl. Mater. Interfaces*, 2020, **12**, 50333–50343.
- 88 N. Patelli, A. Migliori, V. Morandi and L. Pasquini, Interfaces within biphasic nanoparticles give a boost to magnesium-based hydrogen storage, *Nano Energy*, 2020, 72, 104654.
- 89 L. P. A. Mooij, A. Baldi, C. Boelsma, K. Shen, M. Wagemaker, Y. Pivak, H. Schreuders, R. Griessen and B. Dam, Interface energy controlled thermodynamics of nanoscale metal hydrides, *Adv. Energy Mater.*, 2011, 1, 754–758.
- 90 Z. Han, H. Chen and S. Zhou, Dissociation and diffusion of hydrogen on defect-free and vacancy defective Mg (0001) surfaces: A density functional theory study, *Appl. Surf. Sci.*, 2017, 394, 371–377.
- 91 S. Bahou, H. Labrim, M. Lakhal, M. Bhihi, B. Hartiti and H. Ez-Zahraouy, Improving desorption temperature and kinetic properties in MgH₂ by vacancy defects: DFT study, *Int. J. Hydrogen Energy*, 2020, 45, 10806–10813.
- 92 G. Li, H. Kobayashi, J. M. Taylor, R. Ikeda, Y. Kubota, K. Kato, M. Takata, T. Yamamoto, S. Toh, S. Matsumura and H. Kitagawa, Hydrogen storage in Pd nanocrystals covered with a metal-organic framework, *Nat. Mater.*, 2014, 13, 802–806.
- 93 A. Baldi, M. Gonzalez-Silveira, V. Palmisano, B. Dam and R. Griessen, Destabilization of the Mg-H System through Elastic Constraints, *Phys. Rev. Lett.*, 2009, **102**, 226102.
- 94 Y. Luo, Q. Wang, J. Li, F. Xu, L. Sun, Y. Zou, H. Chu, B. Li and K. Zhang, Enhanced hydrogen storage/sensing of metal hydrides by nanomodification, *Mater. Today Nano*, 2020, 9, 100071.
- 95 R. W. P. Wagemans, J. H. van Lenthe, P. E. de Jongh, A. J. van Dillen and K. P. de Jong, Hydrogen storage in magnesium clusters: quantum chemical study, *J. Am. Chem. Soc.*, 2005, **127**, 16675–16680.
- 96 N. S. Norberg, T. S. Arthur, S. J. Fredrick and A. L. Prieto, Size-dependent hydrogen storage properties of Mg nanocrystals prepared from solution, *J. Am. Chem. Soc.*, 2011, 133, 10679–10681.
- 97 X. Zhang, Y. Liu, Z. Ren, X. Zhang, J. Hu, Z. Huang, Y. Lu, M. Gao and H. Pan, Realizing 6.7 wt% reversible storage of hydrogen at ambient temperature with non-confined ultrafine magnesium hydrides, *Energy Environ. Sci.*, 2021, 14, 2302–2313.
- 98 M. Rueda, L. M. Sanz-Moral and Á. Martín, Innovative methods to enhance the properties of solid hydrogen storage materials based on hydrides through

- nanoconfinement: A review, J. Supercrit. Fluids, 2018, 141, 198-217.
- 99 M. Konarova, A. Tanksale, J. Norberto Beltramini and G. Oing Lu, Effects of nano-confinement on the hydrogen desorption properties of MgH2, Nano Energy, 2013, 2, 98-104.
- 100 H. Liang, D. Chen, M. Chen, W. Li and R. Snyders, Study of the synthesis of PMMA-Mg nanocomposite for hydrogen storage application, Int. J. Hydrogen Energy, 2020, 45, 4743-4753.
- 101 H. Liang, D. Chen, D. Thiry, W. Li, M. Chen and R. Snyders, Efficient hydrogen storage with the combination of metal Mg and porous nanostructured material, Int. J. Hydrogen Energy, 2019, 44, 16824-16832.
- 102 V. Berezovets, A. Kytsya, I. Zavaliy and V. A. Yartys, Kinetics and mechanism of MgH₂ hydrolysis in MgCl₂ solutions, Int. J. Hydrogen Energy, 2021, 46, 40278-40293.
- 103 Z. Liu, J. Zhong, H. Leng, G. Xia and X. Yu, Hydrolysis of Mg-based alloys and their hydrides for efficient hydrogen generation, Int. J. Hydrogen Energy, 2021, 46, 18988-19000.